

**INVESTIGATING HOW ENERGY USE PATTERNS SHAPE INDOOR
NANOAEROSOL DYNAMICS IN A NET-ZERO ENERGY HOUSE**

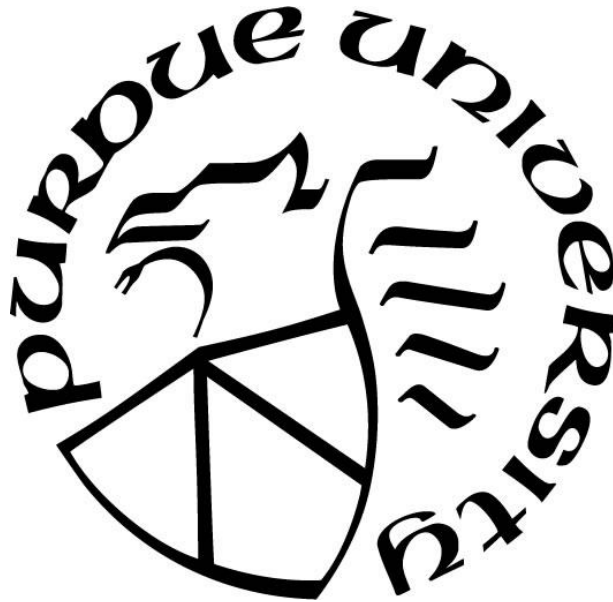
by
Jinglin Jiang

A Thesis

Submitted to the Faculty of Purdue University

In Partial Fulfillment of the Requirements for the degree of

Master of Science in Civil Engineering



Lyles School of Civil Engineering

West Lafayette, Indiana

December 2018

**THE PURDUE UNIVERSITY GRADUATE SCHOOL
STATEMENT OF COMMITTEE APPROVAL**

Dr. Brandon E. Boor, Chair

Lyles School of Civil Engineering

Dr. Panagiota Karava

Lyles School of Civil Engineering

Dr. Eckhard A. Groll

School of Mechanical Engineering

Approved by:

Dr. Dulcy M. Abraham

Head of the Graduate Program

ACKNOWLEDGMENTS

I would first like to thank my thesis advisor, Dr. Brandon E. Boor, for the valuable advice, guidance, and support on my research. I sincerely thank the Whirlpool Corporation for providing access to the ReNEWW House and the cooperation of the residents of the ReNEWW House. I would also like to acknowledge the help of Jason Schneemann, Stephen Caskey, Tianren Wu and Danielle Wagner.

TABLE OF CONTENTS

LIST OF TABLES	6
LIST OF FIGURES	7
ABSTRACT	10
1. INTRODUCTION	12
1.1 Human health impacts of indoor nanoaerosols	12
1.2 Indoor nanoaerosols in net-zero energy buildings	13
1.3 Smart energy and temperature monitoring and indoor nanoaerosol dynamics.....	14
2. METHODS	16
2.1 Overview of the field campaign.....	16
2.2 Site description: Purdue ReNEWW House.....	16
2.3 Sampling protocol.....	19
2.4 Aerosol instrumentation.....	20
2.5 Energy monitoring system	22
2.6 Smart thermostats.....	22
2.7 HVAC operational conditions.....	23
2.8 Data analysis	24
2.9 Aerosol physics-based material balance model	25
2.9.1 Schematic of the material balance model	25
2.9.2 Source and loss processes under four HVAC system operational conditions	26
2.9.3 Estimation of nanoaerosol loss rates.....	27
2.9.4 Estimation of nanoaerosol source rates	28
2.10 Supplemental measurements to determine selected material balance parameters.....	28
2.10.1 Infiltration and interzonal volumetric airflow rates	28
2.10.2 HVAC system volumetric airflow rates	29
2.10.3 Nanoaerosol removal efficiency of kitchen range hood.....	30
2.10.4 Outdoor aerosol size distributions.....	31
3. RESULTS AND DISCUSSION	33
3.1 Aerosol concentrations and size distributions.....	33
3.2 HVAC system run-time	54

3.3 Nanoaerosol loss rates.....	55
3.4 Nanoaerosol source rates	57
4. CONCLUSIONS	59
REFERENCES	60
VITA.....	64

LIST OF TABLES

Table 2.1 Volumetric airflow rates.	29
Table 3.1 Number of indoor cooking events as determined by energy monitoring data.	37
Table 3.2 Parameters of the indoor aerosol number, surface area, volume and mass size distributions for the four electrical kitchen appliances.	45
Table 3.3 Parameters of the indoor aerosol number, surface area, volume and mass size distributions for different periods of the day.	53
Table 3.4 Number of loss rates calculated for each HVAC system operational condition.	55

LIST OF FIGURES

Figure 2.1 Purdue ReNEWW House.....	17
Figure 2.2 The kitchen on the main floor of the ReNEWW House.....	18
Figure 2.3 Air handling unit (AHU) in the basement of the ReNEWW House.....	18
Figure 2.4 Energy recovery ventilator (ERV) in the basement of the ReNEWW House.....	19
Figure 2.5 OPS (left) and NanoScan SMPS (right).....	21
Figure 2.6 The uHoo device.....	22
Figure 2.7 The Ecobee3 lite thermostat.....	23
Figure 2.8 Schematic for the material balance model of the ReNEWW House.....	25
Figure 3.1 Time series plot for: (a.) power usage of cooktop, AHU, and ERV; (b.) setpoint and room temperatures and heating status; (c.) aerosol size-integrated number and mass concentrations; (d.) aerosol number size distributions ($dN/d\log D_p$, cm^{-3}) from 10 nm to 10,000 nm; and (e.) aerosol mass size distributions ($dM/d\log D_p$, $\mu\text{g m}^{-3}$) from 10 nm to 10,000 nm for two hours following a cooking event with the cooktop.....	34
Figure 3.2 Time series plot for: (a.) power usage of toaster, AHU, and ERV; (b.) setpoint and room temperatures and heating status; (c.) aerosol size-integrated number and mass concentrations; (d.) aerosol number size distributions ($dN/d\log D_p$, cm^{-3}) from 10 nm to 10,000 nm; and (e.) aerosol mass size distributions ($dM/d\log D_p$, $\mu\text{g m}^{-3}$) from 10 nm to 10,000 nm for three hours following a cooking event with the toaster.....	35
Figure 3.3 Diurnal indoor and outdoor nanoaerosol number concentrations on (a.) weekdays and (b.) weekends. The red line, yellow line, and the grey region represent the median, mean, and the interquartile range, respectively. The dashed line is median outdoor particle concentration.....	36
Figure 3.4 Size-integrated indoor nanoaerosol number concentrations from 10 nm to 100 nm during the active emission periods of different electrical kitchen appliances and during background periods in the house. Box plots represent interquartile range, whiskers represent the 5th and 95th percentiles, and markers represent outliers. Note: one point at $9.6 \times 10^4 \text{ cm}^{-3}$ is excluded from the oven boxplot for better visualization.....	38
Figure 3.5 Median indoor aerosol number size distributions ($dN/d\log D_p$, cm^{-3}) from 10 nm to 10,000 nm under the operation of different electrical kitchen appliances and during background periods (no emissions).....	40
Figure 3.6 Median aerosol size distributions for the cooktop from 10 nm to 10,000 nm: (a.) aerosol number size distribution ($dN/d\log D_p$, cm^{-3}); (b.) aerosol surface area distribution ($dS/d\log D_p$, $\mu\text{m}^2 \text{ cm}^{-3}$); (c.) aerosol volume distribution ($dV/d\log D_p$, $\mu\text{m}^3 \text{ cm}^{-3}$); (d.) aerosol mass distribution ($dM/d\log D_p$, $\mu\text{g m}^{-3}$). Dashed black curves show the log-normal fitting of the measured distributions and dashed pink, blue, and red curves denote the individual modes. The geometric	

mean diameter ($Mode_i$), geometric standard deviation (σ_i), and amplitude (N_i , S_i , V_i , M_i) for each are presented. 41

Figure 3.7 Median aerosol size distributions for the oven from 10 nm to 10,000 nm: (a.) aerosol number size distribution ($dN/d\log D_p$, cm^{-3}); (b.) aerosol surface area distribution ($dS/d\log D_p$, $\mu\text{m}^2 \text{cm}^{-3}$); (c.) aerosol volume distribution ($dV/d\log D_p$, $\mu\text{m}^3 \text{cm}^{-3}$); (d.) aerosol mass distribution ($dM/d\log D_p$, $\mu\text{g m}^{-3}$). Dashed black curves show the log-normal fitting of the measured distributions and dashed pink, blue, and red curves denote the individual modes. The geometric mean diameter ($Mode_i$), geometric standard deviation (σ_i), and amplitude (N_i , S_i , V_i , M_i) for each are presented. 42

Figure 3.8 Median aerosol size distributions for the toaster from 10 nm to 10,000 nm: (a.) aerosol number size distribution ($dN/d\log D_p$, cm^{-3}); (b.) aerosol surface area distribution ($dS/d\log D_p$, $\mu\text{m}^2 \text{cm}^{-3}$); (c.) aerosol volume distribution ($dV/d\log D_p$, $\mu\text{m}^3 \text{cm}^{-3}$); (d.) aerosol mass distribution ($dM/d\log D_p$, $\mu\text{g m}^{-3}$). Dashed black curves show the log-normal fitting of the measured distributions and dashed pink, blue, and red curves denote the individual modes. The geometric mean diameter ($Mode_i$), geometric standard deviation (σ_i), and amplitude (N_i , S_i , V_i , M_i) for each are presented. 43

Figure 3.9 Median aerosol size distributions for the microwave oven from 10 nm to 10,000 nm: (a.) aerosol number size distribution ($dN/d\log D_p$, cm^{-3}); (b.) aerosol surface area distribution ($dS/d\log D_p$, $\mu\text{m}^2 \text{cm}^{-3}$); (c.) aerosol volume distribution ($dV/d\log D_p$, $\mu\text{m}^3 \text{cm}^{-3}$); (d.) aerosol mass distribution ($dM/d\log D_p$, $\mu\text{g m}^{-3}$). Dashed black curves show the log-normal fitting of the measured distributions and dashed pink, blue, and red curves denote the individual modes. The geometric mean diameter ($Mode_i$), geometric standard deviation (σ_i), and amplitude (N_i , S_i , V_i , M_i) for each are presented. 44

Figure 3.10 Median indoor aerosol number size distributions ($dN/d\log D_p$, cm^{-3}) from 10 nm to 10,000 nm for different periods of the day. 47

Figure 3.11 Median aerosol size distributions during 23:00 to 7:00 from 10 nm to 10,000 nm: (a.) aerosol number size distribution ($dN/d\log D_p$, cm^{-3}); (b.) aerosol surface area distribution ($dS/d\log D_p$, $\mu\text{m}^2 \text{cm}^{-3}$); (c.) aerosol volume distribution ($dV/d\log D_p$, $\mu\text{m}^3 \text{cm}^{-3}$); (d.) aerosol mass distribution ($dM/d\log D_p$, $\mu\text{g m}^{-3}$). Dashed black curves show the log-normal fitting of the measured distributions and dashed pink, blue, and red curves denote the individual modes. The geometric mean diameter ($Mode_i$), geometric standard deviation (σ_i), and amplitude (N_i , S_i , V_i , M_i) for each are presented. 48

Figure 3.12 Median aerosol size distributions during 07:00 to 12:00 from 10 nm to 10,000 nm: (a.) aerosol number size distribution ($dN/d\log D_p$, cm^{-3}); (b.) aerosol surface area distribution ($dS/d\log D_p$, $\mu\text{m}^2 \text{cm}^{-3}$); (c.) aerosol volume distribution ($dV/d\log D_p$, $\mu\text{m}^3 \text{cm}^{-3}$); (d.) aerosol mass distribution ($dM/d\log D_p$, $\mu\text{g m}^{-3}$). Dashed black curves show the log-normal fitting of the measured distributions and dashed pink, blue, and red curves denote the individual modes. The geometric mean diameter ($Mode_i$), geometric standard deviation (σ_i), and amplitude (N_i , S_i , V_i , M_i) for each are presented. 49

Figure 3.13 Median aerosol size distributions during 12:00 to 14:00 from 10 nm to 10,000 nm: (a.) aerosol number size distribution ($dN/d\log D_p$, cm^{-3}); (b.) aerosol surface area distribution ($dS/d\log D_p$, $\mu\text{m}^2 \text{cm}^{-3}$); (c.) aerosol volume distribution ($dV/d\log D_p$, $\mu\text{m}^3 \text{cm}^{-3}$); (d.) aerosol mass

distribution ($dM/d\log D_p$, $\mu\text{g m}^{-3}$). Dashed black curves show the log-normal fitting of the measured distributions and dashed pink, blue, and red curves denote the individual modes. The geometric mean diameter ($Mode_i$), geometric standard deviation (σ_i), and amplitude (N_i , S_i , V_i , M_i) for each are presented. 50

Figure 3.14 Median aerosol size distributions during 14:00 to 17:00 from 10 nm to 10,000 nm: (a.) aerosol number size distribution ($dN/d\log D_p$, cm^{-3}); (b.) aerosol surface area distribution ($dS/d\log D_p$, $\mu\text{m}^2 \text{cm}^{-3}$); (c.) aerosol volume distribution ($dV/d\log D_p$, $\mu\text{m}^3 \text{cm}^{-3}$); (d.) aerosol mass distribution ($dM/d\log D_p$, $\mu\text{g m}^{-3}$). Dashed black curves show the log-normal fitting of the measured distributions and dashed pink, blue, and red curves denote the individual modes. The geometric mean diameter ($Mode_i$), geometric standard deviation (σ_i), and amplitude (N_i , S_i , V_i , M_i) for each are presented. 51

Figure 3.15 Median aerosol size distributions during 17:00 to 23:00 from 10 nm to 10,000 nm: (a.) aerosol number size distribution ($dN/d\log D_p$, cm^{-3}); (b.) aerosol surface area distribution ($dS/d\log D_p$, $\mu\text{m}^2 \text{cm}^{-3}$); (c.) aerosol volume distribution ($dV/d\log D_p$, $\mu\text{m}^3 \text{cm}^{-3}$); (d.) aerosol mass distribution ($dM/d\log D_p$, $\mu\text{g m}^{-3}$). Dashed black curves show the log-normal fitting of the measured distributions and dashed pink, blue, and red curves denote the individual modes. The geometric mean diameter ($Mode_i$), geometric standard deviation (σ_i), and amplitude (N_i , S_i , V_i , M_i) for each are presented. 52

Figure 3.16 Temporal power usage profiles of the ReNEWW House AHU and ERV from April 03, 2018 to May 06, 2018. Colorbar indicates power consumption in W. 54

Figure 3.17 Median and mean diurnal run-time profile of the ReNEWW House AHU and ERV. 55

Figure 3.18 Kernel density functions of size-integrated nanoaerosol loss rates (h^{-1}) under three HVAC system operational conditions. 56

Figure 3.19 Size-integrated nanoaerosol source rates for the HVAC system under different operational conditions and each electrical kitchen appliance. 58

Figure 3.20 Kernel density functions of size-integrated nanoaerosol source rates (h^{-1}) for the HVAC system under different operational conditions and each electrical kitchen appliance. 58

ABSTRACT

Author: Jiang, Jinglin. MS

Institution: Purdue University

Degree Received: December 2018

Title: Investigating How Energy Use Patterns Shape Indoor Nanoaerosol Dynamics in a Net-Zero Energy House

Committee Chair: Dr. Brandon E. Boor

Research on net-zero energy buildings (NZEBS) has been largely centered around improving building energy performance, while little attention has been given to indoor air quality. A critically important class of indoor air pollutants are nanoaerosols – airborne particulate matter smaller than 100 nm in size. Nanoaerosols penetrate deep into the human respiratory system and are associated with deleterious toxicological and human health outcomes. An important step towards improving indoor air quality in NZEBs is understanding how occupants, their activities, and building systems affect the emissions and fate of nanoaerosols. New developments in smart energy monitoring systems and smart thermostats offer a unique opportunity to track occupant activity patterns and the operational status of residential HVAC systems. In this study, we conducted a one-month field campaign in an occupied residential NZEB, the Purdue ReNEWW House, to explore how energy use profiles and smart thermostat data can be used to characterize indoor nanoaerosol dynamics. A Scanning Mobility Particle Sizer and Optical Particle Sizer were used to measure indoor aerosol concentrations and size distributions from 10 to 10,000 nm. AC current sensors were used to monitor electricity consumption of kitchen appliances (cooktop, oven, toaster, microwave, kitchen hood), the air handling unit (AHU), and the energy recovery ventilator (ERV). Two Ecobee smart thermostats informed the fractional amount of supply airflow directed to the basement and main floor. The nanoaerosol concentrations and energy use profiles were integrated with an aerosol physics-based material balance model to quantify nanoaerosol source and loss processes. Cooking activities were found to dominate the emissions of indoor nanoaerosols, often elevating indoor nanoaerosol concentrations beyond 10^4 cm^{-3} . The emission rates for different cooking appliances varied from 10^{11} h^{-1} to 10^{14} h^{-1} . Loss rates were found to be significantly different between AHU/ERV off and on conditions, with median loss rates of 1.43 h^{-1} to 3.68 h^{-1} , respectively. Probability density functions of the source and loss rates for different scenarios will be used in

Monte Carlo simulations to predict indoor nanoaerosol concentrations in NZEBs using only energy consumption and smart thermostat data.

1. INTRODUCTION

1.1 Human health impacts of indoor nanoaerosols

Airborne particulate matter, or aerosols, represent a fascinating mixture of tiny, suspended liquid and solid particles that can span in size from a single nanometer to tens of micrometers. A critically important class of indoor aerosols are nanoaerosols (or ultrafine particles, UFPs) – particles smaller than 100 nm in size. Nanoaerosols are the most numerous particles in the indoor and outdoor atmosphere and exhibit diverse physiochemical properties. They dominate particle number size distributions, have very high surface area to mass ratios, and can exist at levels ranging from 10^3 to $> 10^6$ cm^{-3} . With each breath of indoor air, we inhale several million nanoaerosols. A significant fraction of indoor nanoaerosols are organic and are produced by common processes, such as O_3 and OH oxidation of volatile organic compounds (VOCs), combustion (natural gas and propane stoves, candles), cooking, and evaporation-condensation of semi-VOCs (SVOCs) (Wallace et al. 2017).

The majority of our respiratory encounters with aerosols occurs indoors, where we spend 80-90% of our time and inhale more than 10,000 L of air every day. Indoor air quality is especially important in residential environments, where Americans spend approximately 69% of their time (Klepeis et al. 2001). Understanding the dynamics of indoor nanoaerosols in buildings and their HVAC systems is necessary to understand the implications for human exposure assessment and health outcomes.

Many studies have demonstrated that inhalation exposure to nanoaerosols is responsible for adverse health effects, including mortality and morbidity due to cardiovascular and respiratory diseases (Peters et al. 1997; Oberdörster 2001; De Hartog et al. 2003; Newby et al. 2015). These nano-sized particles penetrate deep into our respiratory systems and preferentially deposit in both the tracheobronchial and alveolar regions of our lungs. Nanoaerosols removed in our head airways can translocate to the brain via the olfactory bulb. Nanoaerosols have been associated with various deleterious toxicological outcomes, such as oxidative stress and chronic inflammation in lung cells. Nanoaerosols are less likely to be cleared from the respiratory tract compared to larger particles,

offering greater opportunities for translocation within the body, such as from lung cells to blood (Panas et al. 2014). Through blood circulation, they will reach organ systems and other sensitive target sites, such as bone marrow, lymph nodes, spleen, and heart (Oberdörster, Oberdörster, and Oberdörster 2005).

1.2 Indoor nanoaerosols in net-zero energy buildings

Buildings account for approximately 40% of total primary energy consumption in the United States and residential buildings are responsible for 22% of the total amount (US Department of Energy 2011). The concept of net zero energy buildings (NZEBs) has been proposed as a means to reduce building energy consumption and mitigate climate change. A NZEB is defined as an energy-efficient building where, on a source energy basis, the actual annual delivered energy is less than or equal to the on-site renewable exported energy (US Department of Energy 2015). To achieve net-zero energy, energy-saving and renewable energy utilization technologies are integrated to reduce the energy consumption and to generate more energy, respectively. Considering the active and passive technologies applied to NZEBs, some unique attributes of NZEBs have the potential to influence indoor nanoaerosol dynamics. For instance, NZEBs are often built with an airtight envelope to minimize infiltration of outdoor air. However, when there are active indoor nanoaerosol emissions in the building, the airtightness could increase the residence time of the nanoaerosols. Furthermore, the HVAC system of a NZEB is typically designed to satisfy the need of the occupants' thermal comfort preferences, without consideration for indoor air quality. Therefore, the operational cycle, or run-time, of the HVAC system may not be sufficient to maintain indoor nanoaerosol concentrations at acceptable levels. The HVAC system could draw outdoor air in when outdoor nanoaerosol concentrations are high or fail to vent indoor air out when there is a significant indoor nanoaerosol source (e.g. cooking or combustion). Therefore, investigating the dynamics indoor nanoaerosols in NZEBs is of great importance.

In recent years, most studies on residential and commercial NZEBs have focused on the energy performance of the building and the thermal comfort of the residents (Voyvodic 2012; Thomas and Duffy 2013; Ascione et al. 2016). Studies have begun to investigate indoor air quality in NZEBs or energy-efficient buildings in terms of carbon dioxide (CO₂), mass concentrations of

particulate matter smaller than $2.5 \mu\text{m}$ in aerodynamic diameter ($\text{PM}_{2.5}$), selected volatile organic compounds (VOCs), and several other gases (Derbez et al. 2014; Ng et al. 2018). However, research on indoor nanoaerosols in residential NZEBs is lacking, especially long-term monitoring (> 1 week) of indoor nanoaerosol concentrations and size distributions.

1.3 Smart energy and temperature monitoring and indoor nanoaerosol dynamics

With the development of the concept of smart buildings, there is an increasing number of smart meters and smart devices applied in residential buildings. Such devices can monitor energy consumption, temperature, relative humidity, and use such data to optimize HVAC control and improve the management of the grid. As of December 2016, over 72 million smart energy meters have been installed in the U.S., covering over 55% of homes (IEI 2016). Recent studies on smart meters have focused on optimal control of the microgrid, load management, and future energy prediction through the data acquired from the smart meters along with other smart devices (Arghira et al. 2012; Diefenderfer, Jansson, and Prescott 2015; Candanedo, Feldheim, and Deramaix 2017). Moreover, energy usage data can indicate the use patterns of electrical appliances to provide more reliable inputs for building energy simulations (Cetin, Tabares-Velasco, and Novoselac 2014).

The increasing deployment of energy and temperature monitoring systems offers an opportunity to explore indoor nanoaerosol dynamics in NZEBs. From the appliance-specific energy usage profiles, the primary source and loss processes of indoor nanoaerosols can be characterized. For example, in a residential NZEB with electrical cooking appliances and absence of indoor combustion sources (e.g. candles), the dominant indoor nanoaerosol emissions are from cooking activities, the time and duration of which can be retrieved from the energy data of kitchen appliances, including the cooktop, oven, toaster, and microwave oven. Meanwhile, the operation of the HVAC system may affect both source and loss mechanisms of indoor nanoaerosols. A fraction of indoor-generated nanoaerosols can be captured by the HVAC filter in the air handling unit (AHU) or exhausted to outdoors through an energy recovery ventilator (ERV), while outdoor nanoaerosols can be vented in with fresh air through the ERV. Energy data coupled with smart thermostat data can indicate the operational status of the HVAC system (AHU and ERV), thus the related source and loss processes can be determined. In this way, we could relate the energy use

profiles of the kitchen appliances and HVAC system to the source and loss processes of indoor nanoaerosols, informing temporal trends in indoor nanoaerosol concentrations and size distributions.

To our knowledge, there is no published research on occupied residential NZEBs that report real-time indoor nanoaerosol concentrations and size distributions or incorporate energy monitoring data to characterize indoor nanoaerosol mechanisms. To fill these gaps in the building science literature, the primary objectives of this project are to characterize the concentrations and size distributions of indoor nanoaerosols in an occupied net zero energy residence and to relate HVAC system and electrical kitchen appliance energy use profiles and smart thermostat data to nanoaerosol source and loss processes. Indoor nanoaerosol concentrations were monitored for a month in the residence, meanwhile, energy monitoring data and thermostat data were also collected. An aerosol physics-based material balance model was developed to characterize source and loss rates under different conditions, informed by the energy usage patterns.

2. METHODS

2.1 Overview of the field campaign

A one-month field measurement campaign was conducted to investigate the relationship between energy use patterns and indoor nanoaerosol dynamics in an occupied net-zero energy residence. The residence is equipped with smart energy monitors and smart thermostats. Two particle sizers were used to monitor indoor aerosol size distributions minute by minute. Two thermostats located on the main floor and the basement can control the AHU status and setpoint temperature separately. An ERV is equipped along with the AHU. In the ERV, heat and moisture are exchanged between exhaust air and outdoor air to preheat/precool the outdoor air. The ERV operated on a preset cycle. During the measurement campaign, four different HVAC system statuses were observed. Energy usage data indicated the usage of kitchen appliances and the HVAC operational condition. As no indoor combustion sources were present, cooking on electrical kitchen appliance was the primary source of indoor nanoaerosols. The HVAC system can deliver nanoaerosols from outdoors and other zones to the main floor, while also transporting nanoaerosols from the main floor to the outdoors and other zone. Nanoaerosols can also be removed by the HVAC filter installed in the AHU. Thus, the HVAC system can act as both a sink and source of nanoaerosols.

An aerosol physics-based material balance model was developed to better characterize indoor nanoaerosol dynamics under different circumstances, which can be determined by the energy usage data. In addition to the contribution of kitchen appliances and the HVAC system, there are other processes that determine the fate of indoor nanoaerosols, such as infiltration, surface deposition, and particle removal through the kitchen hood. To determine parameters linked to these processes, supplemental measurements were conducted following the completion of the one-month field campaign.

2.2 Site description: Purdue ReNEWW House

The ReNEWW (Retrofitted Net-zero Energy, Water & Waste) House, located in West Lafayette, Indiana, near Purdue University's campus, was originally built in 1928. Retrofits have been made

by the Whirlpool Corporation along with Purdue University to achieve net-zero energy, net-zero water, and net-zero waste since 2013.



Figure 2.1 Purdue ReNEW House.

The house is located at 40.431749, -86.911678, which is classified as Climate Zone 5A (Cool Humid) according to ANSI/ASHRAE Standard 169-2013 (ASHRAE 2013). The house has a total conditioned area of 2864 ft² and a total conditioned volume of 24086 ft³. Three adult residents occupy the house. The house has two floors above ground and one floor below ground. On the main floor, there is a living room, a dining room, a kitchen, a bathroom, and an office. A biofiltration unit, the Purdue Biowall, is installed in the living room to investigate its potential in removing VOCs and improving indoor air quality. The kitchen is equipped with electrical cooking appliances such as an electric induction cooktop, oven, toaster, and microwave oven, which makes it possible to track indoor cooking events through electrical energy monitoring. The second floor has another bathroom and three bedrooms. The AHU and ERV and equipment for other research activities are located in the basement.



Figure 2.2 The kitchen on the main floor of the ReNEWW House.



Figure 2.3 Air handling unit (AHU) in the basement of the ReNEWW House.



Figure 2.4 Energy recovery ventilator (ERV) in the basement of the ReNEWW House.

From October 2013 to August 2015, the ReNEWW House was renovated to become a net-zero energy house. Net-zero water and waste will be reached in future phases. The two-year renovation project included two phases. The first phase determined the energy profile of the original house, beginning in October 2013 and lasting for a year. In the second phase, retrofits were made to achieve net-zero energy. Thermal insulation of the building envelope was improved by replacing windows with a higher thermal resistance, upgrading wall and roof cavities, and applying a spray foam throughout the exterior walls. In addition, a 7 kWp solar photovoltaic–thermal (PV-T) system was installed on the western roof and a 1 kWp traditional PV array was installed on the southern roof. To improve the efficiency of the heating and cooling system, ground-source heat pumps were installed (Caskey, Bowler, and Groll 2016).

2.3 Sampling protocol

The field campaign included one-month of indoor air sampling from April 03 to May 04, 2018 at a central location on the main floor of the ReNEWW House between the kitchen and living room. Supplemental measurements were conducted during the following months, including: outdoor nanoaerosol size distributions, nanoaerosol removal efficiency of the kitchen hood, volumetric airflow rates of HVAC supply and return vents, infiltration rate, and inter-zonal airflow rates.

During the measurement campaign, the residents followed their typical routines. Indoor nanoaerosols were passively sampled by the instruments and energy usage data were gathered by existing data acquisition infrastructure. Overall, the campaign did not have an impact on the normal daily life of the occupants. On the other hand, with the energy usage data we collected through smart meters, we can find out what appliance was operated at a certain time and then infer what event happened in the house at that time. Following this approach, we can exclude the use of activity pattern surveys or questionnaires.

2.4 Aerosol instrumentation

A Scanning Mobility Particle Sizer (SMPS) (NanoScan SMPS, Model 3910, TSI Inc, Shoreview, MN, USA) was used to measure nanoaerosol size distributions in the electrical mobility diameter range of 10 to 420 nm across thirteen size channels. It was operated in SCAN mode, which provides real-time size distributions with a time resolution of 1 minute. The NanoScan SMPS contains an inlet cyclone, a unipolar charger, a radial differential mobility analyzer (RDMA), and an isopropyl-based condensation particle counter (iCPC). The inlet cyclone removes aerosols greater than 550 nm. The sample aerosols is then charged via the unipolar charger to reach a consistent charge state. Inside the RDMA, an electrical field is created to force the particles to move through the gas in which they are suspended and then the particles with a given electrical mobility will exit through the monodisperse outlet and enter the iCPC. The number of particles in each size bin is counted by the iCPC. The iCPC can provide accurate counting statistics at low and high concentrations.

The NanoScan SMPS can underestimate the concentration of particles with a diameter larger than 200 nm, likely because the particle size is close to the upper size-specific limit of the instrument. In addition, the inlet cyclone of the NanoScan SMPS can break apart weakly linked aggregate particles, thus the modes may shift to smaller sizes and the concentration of larger sizes would drop (Yamada, Takaya, and Ogura 2015). A similar phenomenon was also observed in our measurements. Considering the limitations of the NanoScan SMPS in measuring larger aerosols, the aerosol size distributions in the electrical mobility diameter range of 150 to 300 nm was estimated through spline interpolation. Furthermore, nanoaerosols smaller than 10 nm may

contribute significantly to total number concentrations, however, they were not measured in the present investigation.

An Optical Particle Sizer (OPS, Model 3330, TSI Inc, Shoreview, MN, USA) was used to measure aerosol size distributions in the optical diameter range of 300 to 10,000 nm across sixteen size channels. It was also set to record real-time size distributions with 1-minute resolution. The OPS is based on the principle of light scattering by particles. A laser beam is focused below the inlet nozzle to illuminate the particles. When particles pass through the beam, they will scatter the light in the form of pulses, through which the particles can be counted and sized simultaneously. The measured optical diameter of the particles assumes that all particles are spherical (dynamic shape factor of unity), which is a different operating principle compared to the NanoScan SMPS (electrical mobility). As the refractive index and dynamic shape factors of these particles are unknown, their composition and morphology of particles may affect the reported size distributions. After sampling, the NanoScan SMPS and OPS data were merged together to obtain a full aerosol size distribution in the diameter range from 10 nm to 10,000 nm.



Figure 2.5 OPS (left) and NanoScan SMPS (right).

In addition to the NanoScan SMPS and OPS, three uHoo devices were placed at different sampling nodes throughout the house: between the kitchen and living area, office, and bedroom. The uHoo device is a WiFi-enabled smart indoor air quality sensor which integrates nine sensors to monitor

temperature, relative humidity, CO₂, PM_{2.5}, total VOCs (TVOCs), nitrogen dioxide (NO₂), carbon monoxide (CO), ozone (O₃), and barometric pressure. Real-time and historical data can be viewed or downloaded from a mobile app.



Figure 2.6 The uHoo device.

2.5 Energy monitoring system

An electrical energy monitoring system was installed at the ReNEWW House to monitor the energy consumption at the electric panel, down to the equipment level. The current of each circuit and the corresponding power consumption is recorded every minute by a custom programmed computer data acquisition system. The electrical monitoring system had an uncertainty of $\pm 2\%$ of the current transducer (CT) rating (Caskey et al. 2016).

2.6 Smart thermostats

To control the HVAC system, two Ecobee3 lite thermostats are installed in the ReNEWW House, one at the main floor and another at the basement. The Ecobee3 lite is a WiFi-enabled smart thermostat, which can be controlled by voice or smart phone remotely to better satisfy occupants' thermal comfort preferences. It can also adjust temperature intuitively based on outdoor weather

conditions, user schedules, desired settings, and data from room sensors to optimize the control of the HVAC system and to provide a more comfortable thermal environment.

From April 03 to April 11, 2018, the setpoint temperature for main floor was maintained at 70°F from 08:30 to 01:00 and at 66°F from 01:00 to 08:30, and the setpoint temperature for basement kept at 67°F from 07:00 to 23:00 and 65°F from 23:00 to 07:00. From April 12 to May 04, 2018, the main floor setpoint temperature was the same as the period above, while the basement setpoint temperature changed to 64°F for the entire day. When the room temperature drops to 0.5°F below the setpoint temperature, the system will call for the heating.



Figure 2.7 The Ecobee3 lite thermostat.

2.7 HVAC operational conditions

During the field measurement campaign, the following four operational conditions of the HVAC system were observed: (1.) AHU off, ERV off; (2.) AHU on, ERV off; (3.) AHU on, ERV on, main floor heating off; (4.) AHU on, ERV on, main floor heating on. The AHU blower can be turned on by calling for heating/cooling from either zone, or when the ERV operates according to its predefined cycle, which is independent of the heating/cooling requirements. When the AHU and ERV are both off, there is no call for heating/cooling within the house. When the AHU is on

and the ERV is off, there must be a call for heating/cooling. When the AHU and ERV are both on, the heating status needs to be determined from the smart thermostat data. During the testing period, only the heating mode was observed. The average outdoor temperature during the campaign was 44°F, more than 20°F lower than the setpoint temperature. The highest daily-average outdoor temperature was 75 °F on May 2nd. The heating mode was not activated for the most time of that day, but there was still no need for cooling. The AHU run-time was the lowest at that time through the observational period.

2.8 Data analysis

Data measured by the NanoScan SMPS and OPS were merged to obtain a continuous indoor aerosol size distribution from 10 nm to 10,000 nm. Aerosol size distributions in size range of 10 nm to 300 nm in electrical mobility diameter are attained from the NanoScan SMPS and 300 nm to 10,000 nm in optical diameter from OPS. Due to the limitation of the sensitivity of the NanoScan SMPS for particles larger than 150 nm in electrical mobility diameter, aerosol size distributions in from 150 nm to 300 nm were estimated by spline interpolation.

To parameterize the aerosol size distributions, a multi-lognormal size distribution function was applied. It can be expressed as the sum of n lognormal size distributions:

$$\frac{dN}{d\log D_p} = \sum_{i=1}^n \frac{N_i}{(2\pi)^{1/2} \log(\sigma_{g,i})} \exp \left[-\frac{(\log D_p - \log \overline{D_{pg,i}})^2}{2 \log^2(\sigma_{g,i})} \right] \quad \text{Eqn.1}$$

where D_p is the aerosol diameter (nm), N_i is the number concentration (cm^{-3}) of mode i , $\sigma_{g,i}$ is the geometric standard deviation of mode i , and $\overline{D_{pg,i}}$ is the geometric mean diameter (nm) of mode i .

Using the above mathematical expression, we can describe a size distribution with only three key parameters. With the assumption that all the aerosols are spherical, the number size distribution

$(\frac{dN}{d\log D_p})$ can be converted to a surface area size distribution $(\frac{dS}{d\log D_p})$, a volume size distribution

$(\frac{dV}{d\log D_p})$ and a mass size distribution $(\frac{dM}{d\log D_p})$, as shown in Equations 2-4.

$$\frac{dS}{d\log D_p} = \pi D_p^2 \frac{dN}{d\log D_p} \quad \text{Eqn.2}$$

$$\frac{dV}{d\log D_p} = \frac{\pi}{6} D_p^3 \frac{dN}{d\log D_p} \quad \text{Eqn.3}$$

$$\frac{dM}{d\log D_p} = \rho \frac{\pi}{6} D_p^3 \frac{dN}{d\log D_p} \quad \text{Eqn.4}$$

2.9 Aerosol physics-based material balance model

2.9.1 Schematic of the material balance model

A material balance model was developed to characterize the dynamics of indoor nanoaerosols. The house is simplified as a two-zone completely mixed flow reactor (CFMR); one zone is the main floor, with an effective volume of 266 m³, and the other zone is the basement, with an effective volume of 232 m³. In this study, we focus on nanoaerosol dynamics on the main floor. It assumed minimal air exchange occurs between main floor and the second floor.

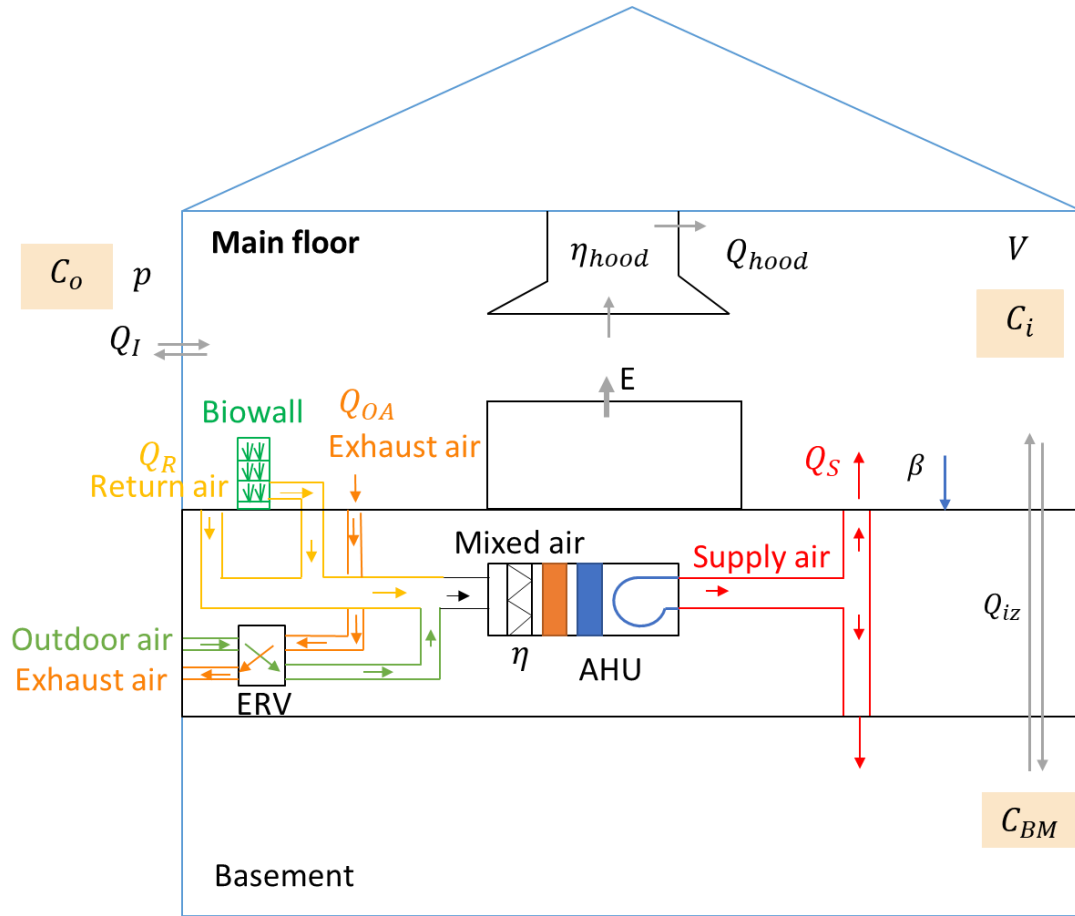


Figure 2.8 Schematic for the material balance model of the ReNEWW House.

$$V \frac{dC_i}{dt} = E + (1 - \eta)(C_o Q_{OA})F + C_{BM} Q_{iz} + p C_o Q_I - C_i \{ \beta V + Q_{OA} + Q_R [1 - (1 - \eta)F] + Q_I + Q_{iz} + \eta_{hood} Q_{hood} \} \quad \text{Eqn.5}$$

In Equation 5, V is effective volume (m^3); E is the emission rate from cooking with electrical kitchen appliances (h^{-1}); η is overall removal efficiency of the HVAC system (-); C_o is outdoor nanoaerosol concentration (cm^{-3}); C_i is the indoor nanoaerosol concentration on the main floor (cm^{-3}); C_{BM} is particle nanoaerosol of the basement (cm^{-3}); Q_{OA} is outdoor volumetric airflow rate provided by the ERV (m^3h^{-1}); Q_R is total return volumetric airflow rate for main floor (m^3h^{-1}); Q_I is the infiltration volumetric airflow rate (m^3h^{-1}); Q_{iz} is the interzonal volumetric airflow rate (m^3h^{-1}); Q_{hood} is the volumetric airflow rate recirculated through the kitchen range hood (m^3h^{-1}); p is penetration factor of outdoor nanoaerosols through the building envelope (-); β is particle deposition loss rate coefficient (-); and η_{hood} is the removal efficiency of the kitchen range hood (-). F is the fraction of air supplied to the main floor to the total supply volumetric airflow rate:

$$F = \frac{Q_S}{Q_R + Q_{OA}} \quad \text{Eqn.6}$$

where Q_S is supply volumetric airflow rate for the main floor (m^3h^{-1}). The material balance model was applied to size-integrated nanoaerosol concentrations from 10 nm to 100 nm, as measured with the NanoScan SMPS. Thus, size-resolved source and loss processes are not reported.

2.9.2 Source and loss processes under four HVAC system operational conditions

In Equation 5, all terms independent of C_i are considered as source terms, otherwise loss terms. Equation 5 can then be written in a simplified form as:

$$\frac{dC_i}{dt} = \frac{S}{V} - C_i L \quad \text{Eqn.7}$$

Equation 5 can be reorganized according to the four different HVAC system operational conditions mentioned in 2.7, which were identified at a given point in time based on the smart energy monitoring and smart thermostat data:

- 1) AHU off, ERV off:

When the AHU and ERV are both off, there is no airflow through the HVAC system.

$$S_1 = E + C_{BM}Q_{iz} + pC_oQ_I \quad \text{Eqn.8}$$

$$L_1 = \beta + \frac{Q_I}{V} + \frac{Q_{iz}}{V} \quad \text{Eqn.9}$$

- 2) AHU on, ERV off:

$$S_2 = E + C_{BM}Q_{iz} + pC_oQ_I \quad \text{Eqn.10}$$

$$L_2 = \beta + \frac{Q_I}{V} + \frac{Q_{iz}}{V} + Q_{R,2}[1 - (1 - \eta)F_2] \quad \text{Eqn.11}$$

As the basement is mostly underneath the ground, the thermal mass of earth can provide good insulation for it. Considering that the basement setpoint temperature is lower than that of the main floor and the building is equipped with high R-value insulation, the heating load of basement can be significantly reduced. During the measurement campaign, the basement did not call for heating. Thus, there was no air supplied to the basement when the ERV was off and the air supplied to the main floor equals to the total return air. Then:

$$F_2 = \frac{Q_{S,2}}{Q_{R,2}} = 1 \quad \text{Eqn.12}$$

$$L_2 = \beta + \frac{Q_I}{V} + \frac{Q_{iz}}{V} + \eta Q_{R,2} \quad \text{Eqn.13}$$

3) AHU on, ERV on, main floor heating off:

$$S_3 = E + (1 - \eta)(C_o Q_{OA,3})F_3 + C_{BM}Q_{iz} + pC_o Q_I \quad \text{Eqn.14}$$

$$L_3 = \beta + \frac{Q_{OA,3}}{V} + \frac{Q_I}{V} + \frac{Q_{iz}}{V} + Q_{R,3}[1 - (1 - \eta)F_3] \quad \text{Eqn.15}$$

4) AHU on, ERV on, main floor heating on:

$$S_4 = E + (1 - \eta)(C_o Q_{OA,4})F_4 + C_{BM}Q_{iz} + pC_o Q_I \quad \text{Eqn.16}$$

$$L_4 = \beta + \frac{Q_{OA,4}}{V} + \frac{Q_I}{V} + \frac{Q_{iz}}{V} + Q_{R,4}[1 - (1 - \eta)F_4] \quad \text{Eqn.17}$$

Although in scenario (3.) and (4.), the expressions for the source and loss terms are same, the volumetric airflow rates of outdoor air, supply air, and return air are different due to the difference in the heating status.

2.9.3 Estimation of nanoaerosol loss rates

The size-integrated nanoaerosol loss rates (10 nm to 100 nm) can be estimated from the decay in nanoaerosol concentrations following an indoor emission event. An analytical solution to Equation 7 is expressed as follows:

$$C_{in} = \left(C_{in,0} - \frac{S}{L} \right) \exp[-L(t - t_0)] + \frac{S}{L} \quad \text{Eqn.18}$$

If the decay period is long enough, a steady-state period when the nanoaerosol concentration does not change with respect to time can be reached. The nanoaerosol concentration at steady-state is

the ratio of the source rate to the loss rate. With $C_{in,0}$, C_{ss} already known, L can be estimated through curve fitting by the least-squares regression method.

$$C_{ss} = \frac{S}{L} \quad \text{Eqn.19}$$

$$C_{in} = (C_{in,0} - C_{ss})exp[-L(t - t_0)] + C_{ss} \quad \text{Eqn.20}$$

2.9.4 Estimation of nanoaerosol source rates

When there are no active indoor nanoaerosol emission sources as determined by the kitchen appliance energy use profiles, the source rates under different HVAC system operational conditions can be determined through Equation 8, 10, 14 and 16, with the measured volumetric airflow rates. When there was an active emission source indoors, the emission rate can be solved through a numerical method based on the nanoaerosol concentration build-up period. The equation below is derived from Eqn. 7, in which $C_{i,t}$ is the indoor nanoaerosol concentration after time t when it began to build up. $\overline{C_{i,t}}$ is the average concentration through time t , and \overline{S}_t is the average source rate through time t . The emission rates of cooking on different electrical kitchen appliances, informed by their respective energy use profiles, can then be determined by comparing \overline{S}_t and the corresponding source rates of the HVAC system.

$$\overline{S}_t = \left(\frac{C_{i,t} - C_{i,0}}{t} + \overline{C_{i,t}}L \right) V \quad \text{Eqn.21}$$

2.10 Supplemental measurements to determine selected material balance parameters

2.10.1 Infiltration and interzonal volumetric airflow rates

The CO₂ decay method was used to determine the infiltration volumetric airflow rate between the main floor and outdoors (Q_I) and the interzonal volumetric airflow rate from basement to the main floor (Q_{iz}). Two experiments were conducted to determine these two parameters. During the experiment, the house was unoccupied in order to avoid the impact of human respiration on indoor CO₂ concentrations.

A 5-lb CO₂ cylinder was used as the source of CO₂ in the house. In the first experiment, it was placed in the kitchen of the main floor. Two mixing fans were used to promote mixing of CO₂. CO₂ was released until its concentration reach approximately 3000 ppm_v. A CO₂ logger (Model:

HOBO MX1102; Onset Computer Corporation, Bourne, MA, USA) was used to monitor the CO₂ concentration at a time resolution of 5 seconds. In the second experiment, the CO₂ cylinder was placed at the center of the basement, with two mixing fans placed in both the kitchen and the basement. Two uHoo devices were used to monitor the CO₂ concentration on the main floor, and one uHoo device and the HOBO CO₂ logger monitored the CO₂ concentration in the basement. The measurements lasted for approximately 2 hours after cessation of CO₂ injection. The CO₂ concentration in each zone will decay due to the leakage across the building interior and envelope. From the decay curve of the CO₂ concentration, the loss rates of each zone can be determined and then the infiltration and interzonal volumetric airflow rate can be estimated.

2.10.2 HVAC system volumetric airflow rates

The volumetric airflow rates are variable under the different HVAC system operational conditions. An air capture hood (Alnor LoFlo Balometer Capture Hood, Model: 6200D, TSI Inc, Shoreview, MN, USA) was used to measure the volumetric airflow rate for each vent under the following three conditions: (1.) Main floor cooling on, basement cooling off, ERV off; (2.) Main floor cooling off, basement cooling off, ERV on; (3.) Main floor cooling on, basement cooling off, ERV on. There are four supply vents in the basement and eight supply vents in the main floor. Two return vents are located near the kitchen and at the stairway, respectively. There is no return vent in the basement. The only exhaust vent is located between the kitchen and breakfast nook and air is exhausted directly to the outdoors through the exhaust vent. The amount of supply, return, and exhaust air were estimated based on the assumption that there was no leakage in the ducts and the HVAC system was well balanced. Since air is also returned from the biofiltration unit, which cannot be measured with the capture hood, the amount of return air is calculated from the difference between the amount of supply air and exhaust air. Table 2.1 lists the measured volumetric airflow rates under different HVAC system conditions.

Table 2.1 Volumetric airflow rates.

Airflow rate [m³h⁻¹]	ERV on, Cooling off	ERV on, Cooling on	ERV off, Cooling on
Supply air to basement	572.6	107.5	--
Supply air to main floor	732.8	775.2	792.5
Return air	1166.1	787.6	792.5
Exhaust air	139.3	95.1	--

2.10.3 Nanoaerosol removal efficiency of kitchen range hood

The nanoaerosol removal efficiency, η , is the fraction of particles removed by the kitchen range hood to the total particles at the inlet of the range hood:

$$\eta = \frac{N_{removed}}{N_{inlet}} = 1 - \frac{N_{outlet}}{N_{inlet}} \quad \text{Eqn.18}$$

As shown in Figure 2.9, one end of a set of two conductive silicon tubes was fixed at the outlet of the range hood, and the other end was extended close to the inlets of the NanoScan SMPS and OPS. One end of another set of two tubes was fixed at the inlet of the range hood, the other end was also placed close to the instruments. The lengths of these four tubes were identical. The inlets of the instruments were switched to connect a different group of tubing to the inlet and outlet of the range hood, alternating between 5 minutes at the hood inlet and 5 minutes at the hood outlet. The concentrations not measured in the other 5 minutes were estimated through interpolation. With the inlet and outlet particle number concentrations, a minute-by-minute nanoaerosol removal efficiency of the kitchen range hood can be obtained. The removal efficiency term was applied in the material balance model when the smart energy monitoring data indicated that the hood was on.



Figure 2.9 Setup of the NanoScan SMPS and OPS to determine the kitchen hood nanoaerosol removal efficiency.

2.10.4 Outdoor aerosol size distributions

A one-week outdoor air sampling period was conducted to determine the outdoor aerosol size distribution. The NanoScan SMPS and OPS were placed on the bench near the kitchen window. A diffusion dryer (Model: 3062, TSI Inc, Shoreview, MN, USA) was used to remove moisture in the outdoor air to prevent condensation in the sample tubes and instruments. The inlets of the instruments were connected to the outlet of the diffusion dryer with conductive silicone tubing. The inlet of the diffusion dryer was connected to conductive silicone tubing that extended to the outdoors. The window was opened slightly to let the tubing pass through. The window opening gap was sealed with foam and tape.



Figure 2.10 Setup of the diffusion dryer, NanoScan SMPS, and OPS for outdoor air sampling.

3. RESULTS AND DISCUSSION

3.1 Aerosol concentrations and size distributions

Figures 3.1 and Figure 3.2 illustrate the temporal variation in the power consumption of two kitchen appliances, ERV, and AHU; setpoint and room temperatures via the smart thermostats; and indoor aerosol concentrations and size distributions from 10 nm to 10,000 nm following the operation of a cooktop and toaster, respectively. Examining the power consumption patterns and aerosol concentrations in Figure 3.1, it can be observed that the concentration began to increase during the active use period of the cooktop and reached a peak concentration approximately 15 minutes after turning on the cooktop. The aerosol size distributions also indicate the emission of aerosols when using the cooktop, especially nanoaerosols – particles with a diameter smaller than 100 nm. Similarly, when using a toaster, a build-up period in nanoaerosol concentrations can also be observed. However, in this case, the concentration increased more rapidly and reached its peak earlier, due to the shorter operation time of the toaster and the toaster being heated faster than the pan on the cooktop. As can be seen in the temperature profile, when the room temperature was 0.5°F lower than the setpoint temperature, heating is turned on until the room temperature reaches the setpoint temperature. When there was a call for heating, or the ERV operated according to its cycle, the AHU turned on. When examining the decay curve in the nanoaerosol concentrations, different loss rates at different HVAC system operational status were found.

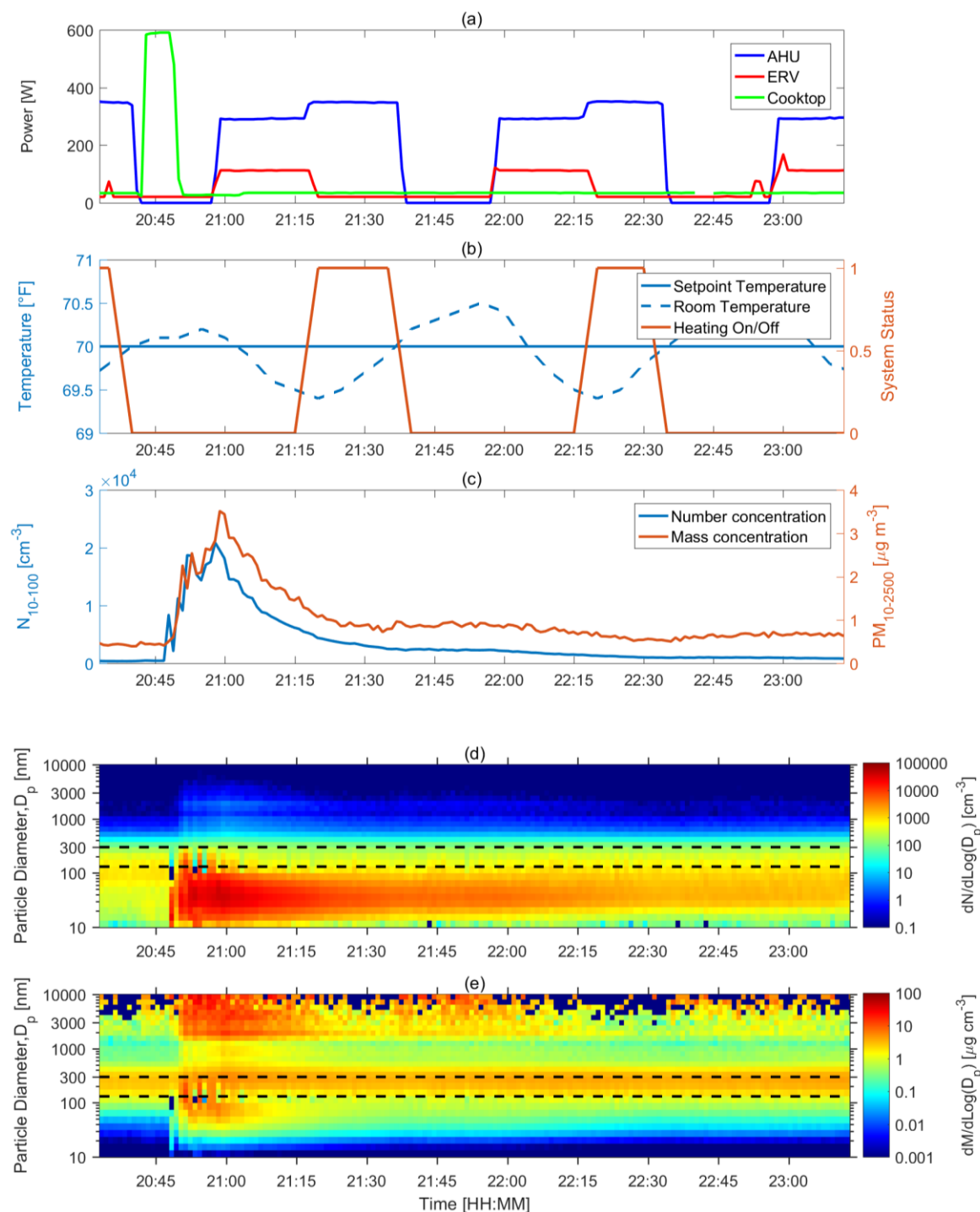


Figure 3.1 Time series plot for: (a.) power usage of cooktop, AHU, and ERV; (b.) setpoint and room temperatures and heating status; (c.) aerosol size-integrated number and mass concentrations; (d.) aerosol number size distributions ($\text{dN/dlog}D_p$, cm^{-3}) from 10 nm to 10,000 nm; and (e.) aerosol mass size distributions ($\text{dM/dlog}D_p$, $\mu\text{g m}^{-3}$) from 10 nm to 10,000 nm for two hours following a cooking event with the cooktop.

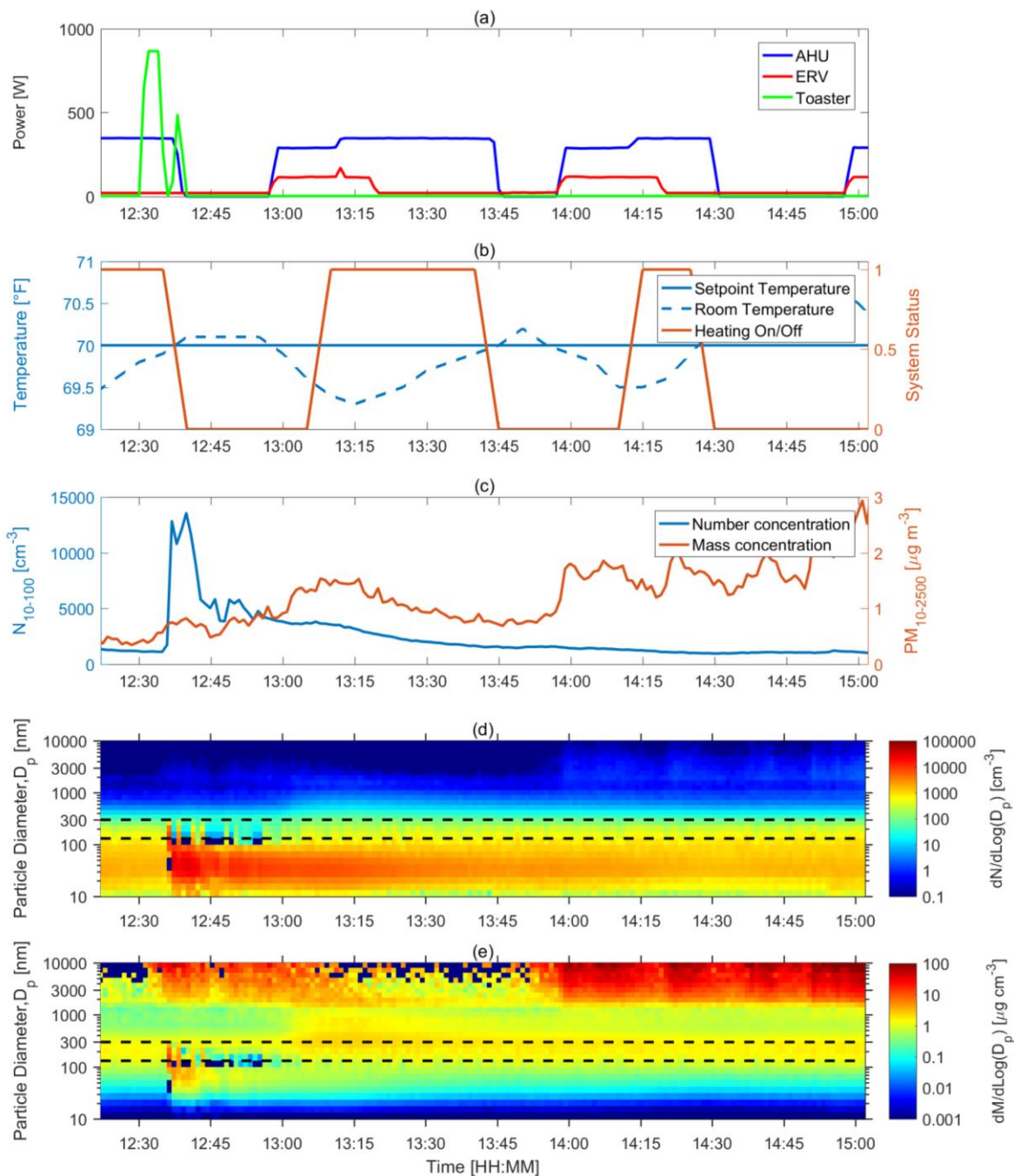
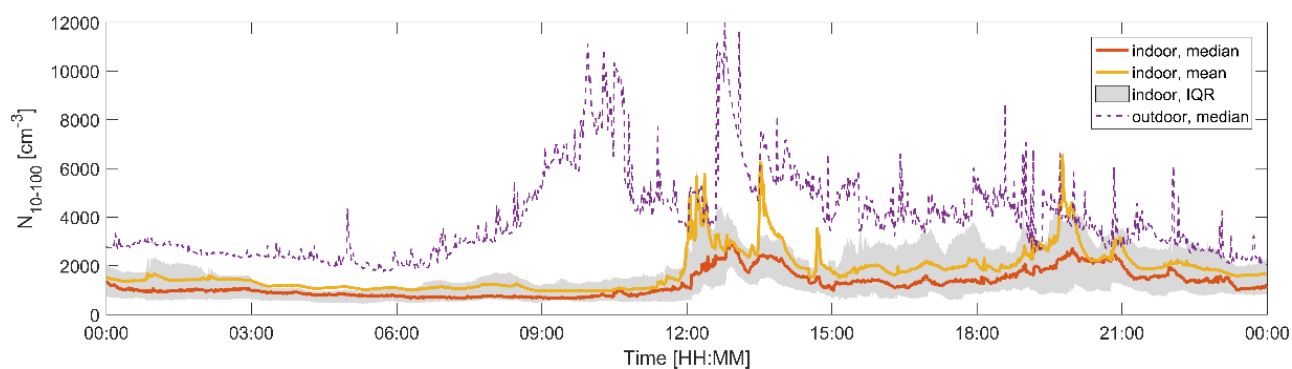


Figure 3.2 Time series plot for: (a.) power usage of toaster, AHU, and ERV; (b.) setpoint and room temperatures and heating status; (c.) aerosol size-integrated number and mass concentrations; (d.) aerosol number size distributions ($dN/d\log D_p$, cm^{-3}) from 10 nm to 10,000 nm; and (e.) aerosol mass size distributions ($dM/d\log D_p$, $\mu\text{g m}^{-3}$) from 10 nm to 10,000 nm for three hours following a cooking event with the toaster.

The indoor and outdoor nanoaerosol concentrations show significant differences between the weekdays and weekends (Figure 3.3), which suggests that the indoor activity patterns and outdoor

sources may vary from weekdays to weekends. On weekdays, the occupants tended to cook in the early afternoon and in the evening, with two peaks in Figure 13(a.) at around 13:00 and 20:00, reaching 10^4 cm^{-3} , respectively. On the weekends, the residents tended to only cook in the evening. Due to the increased traffic on campus during the weekdays, there were more nanoaerosols generated by vehicles outdoors. By contrast, on weekends, the outdoor nanoaerosols remained at lower concentration, approximately $3 \times 10^3 \text{ cm}^{-3}$.

(a.) weekday



(b.) weekend

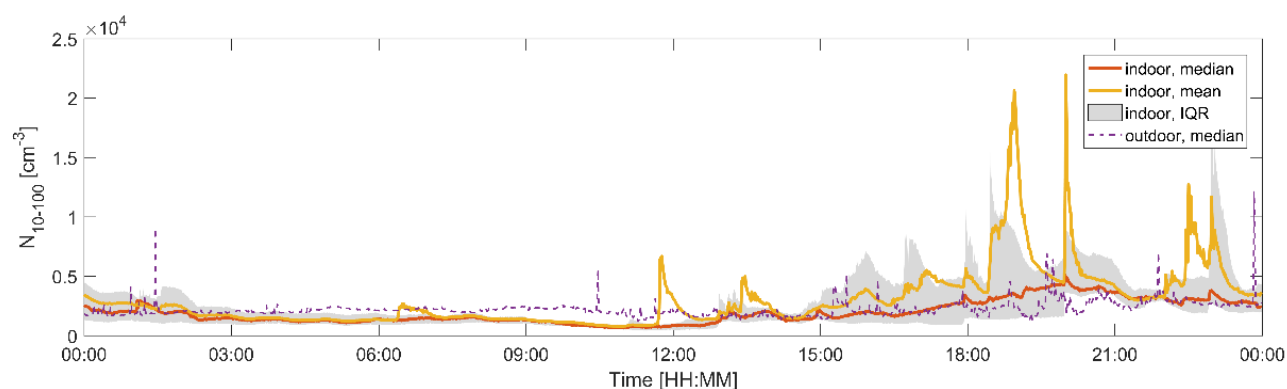


Figure 3.3 Diurnal indoor and outdoor nanoaerosol number concentrations on (a.) weekdays and (b.) weekends. The red line, yellow line, and the grey region represent the median, mean, and the interquartile range, respectively. The dashed line is median outdoor particle concentration.

The figures above demonstrate that indoor cooking activities can strongly influence indoor nanoaerosol concentrations. To further explore the difference between different cooking activities, aerosol size distributions and concentrations for four cooking appliances frequently used in the ReNEW House were investigated. Through the one-month campaign, a total number of 86 cooking events were observed based on the energy use profiles. Table 1 summarizes all cooking

events, as well as indoor nanoaerosol peaks with unknown sources. Such peaks may be due to other indoor events, such as secondary organic aerosol formation due to terpene ozonolysis, which cannot be detected solely by energy monitoring. These unexpected peaks only account 8% of all indoor events. Thus, we conclude that cooking activities are the most important indoor source of nanoaerosols in the electrical mobility range of 10 nm to 100 nm in the ReNEW House.

Table 3.1 Number of indoor cooking events as determined by energy monitoring data.

Events	Number
Cooktop	17
Oven	10
Toaster	21
Microwave oven	32
Cooktop + toaster	3
Cooktop + toaster + oven	2
Toaster + oven	1
Unexpected peaks	7

Figure 3.4 shows the difference among nanoaerosol concentrations for cooking on the four electrical kitchen appliances in the ReNEW House. The nanoaerosol concentration produced when using oven was the highest, with a median value at $6.4 \times 10^3 \text{ cm}^{-3}$, followed by the cooktop and the toaster. When the microwave oven was used, the nanoaerosol concentration was slightly higher than background levels in the house, at around $1.5 \times 10^3 \text{ cm}^{-3}$. Operational temperature differences among the electrical appliances and duration of operation may explain the difference in nanoaerosol concentrations. The oven and the cooktop were often used for a much longer period than the toaster and microwave oven, so more nanoaerosols may be emitted during that period. The temperature of cooktop, toaster and oven in operation can be higher than microwave oven, so microwave oven generates less nanoaerosols. In addition to operational time and temperature, cooking style and food type can also affect the nanoaerosol concentration (Buonanno, Morawska, and Stabile 2009). The background nanoaerosol concentration, with a median value at 946.2 cm^{-3} , when there were no emissions in this residential NZEB was much lower than concentrations reported in typical residences (Wallace 2006; Bhangar et al. 2011), while the concentration during cooking is comparable to values reported in previous studies (Wallace et al. 2008; Zhang et al. 2010). Even though the background indoor nanoaerosol concentrations in the ReNEW House were below those reported for residential buildings in the literature, indoor activities such as cooking can still elevate nanoaerosol concentrations to above $5 \times 10^3 \text{ cm}^{-3}$.

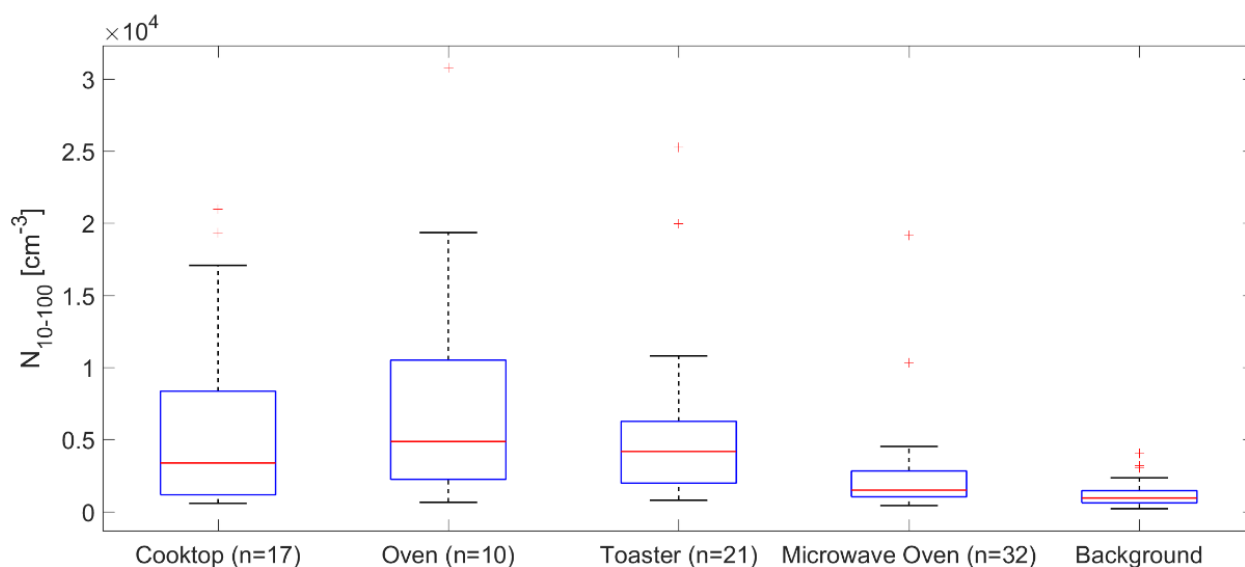


Figure 3.4 Size-integrated indoor nanoaerosol number concentrations from 10 nm to 100 nm during the active emission periods of different electrical kitchen appliances and during background periods in the house. Box plots represent interquartile range, whiskers represent the 5th and 95th percentiles, and markers represent outliers. Note: one point at $9.6 \times 10^4 \text{ cm}^{-3}$ is excluded from the oven boxplot for better visualization.

Figure 3.5 illustrates the difference in aerosol number size distributions for four different kitchen appliances and background periods when there were no emissions. Figures 3.6-3.9 provide more details on the number, surface area, volume, and mass size distributions for each appliance. Consistent with the concentrations, the magnitude $dN/d\log D_p$ was highest when using the oven, followed by the cooktop and toaster, and magnitude of $dN/d\log D_p$ for the microwave oven was slightly greater than background periods in the house.

The parameters of the multi-lognormal distribution function for indoor aerosols when different kitchen appliance was active are listed in Table 3.2. All the number size distributions can be fitted to three modes. For cooktop and oven, the two smaller modes in Aitken mode are close to each other. Aerosol number size distribution for cooktop is dominated by a mode at 39.3 nm, with the number concentration at 2602 cm^{-3} and the geometric standard deviation at 2.17. Compared with cooktop, the number size distributions of oven, toaster are dominated by a smaller mode, with the diameter at around 30 nm. From Figure 3.6-3.9, it can be observed that the distributions for cooktop

and toaster are more uniform than oven, and the modes for toaster are shifted to smaller size ranges compared to cooktop and oven. The surface area size distributions are tri-modal distribution, with three modes located at Aitken mode, accumulation mode and coarse mode, respectively. Modes at 162.7 nm, 175.5 nm and 142.3 nm in accumulation mode contribute the most to the surface area distributions for cooktop, toaster and microwave oven, respectively, while the mode at 65.3 nm in Aitken mode dominates the distribution of oven. The surface area concentration of the smallest mode for microwave oven is too low to be observed from the plot. Volume and mass size distributions behave similar. The distributions can be parameterized as bi-modal or tri-modal distribution, with one or two mode below 250 nm and a larger mode at around 10,000 nm. For cooktop, the volume and mass concentrations in size bins between 3,000 nm and 10,000 nm are much higher than other appliances, indicating that the cooktop can generate more coarse aerosols. The distributions among the other three appliances do not show significant difference, the resuspension of aerosols caused by residents' movement during cooking can contribute to the mode around 10,000 nm.

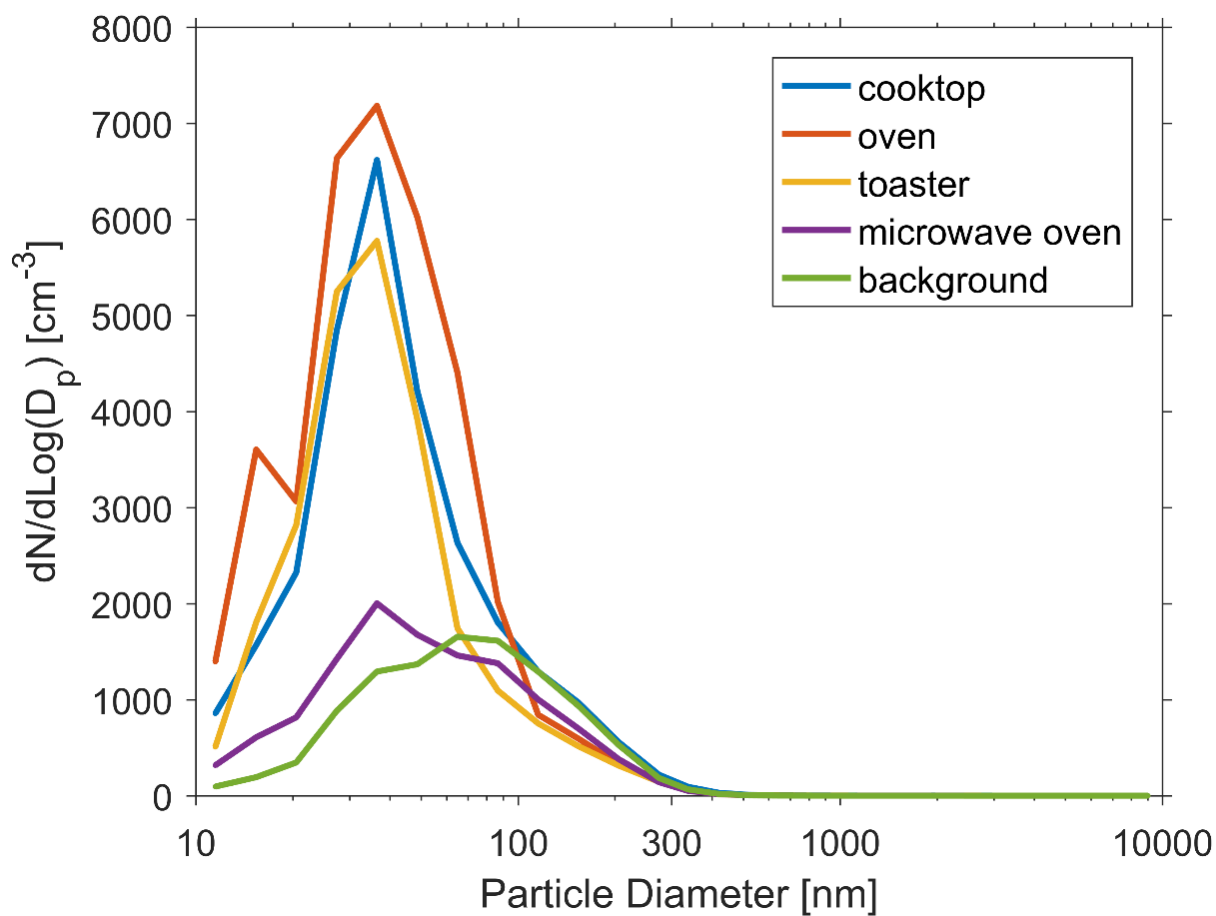


Figure 3.5 Median indoor aerosol number size distributions ($dN/d\log D_p$, cm^{-3}) from 10 nm to 10,000 nm under the operation of different electrical kitchen appliances and during background periods (no emissions).

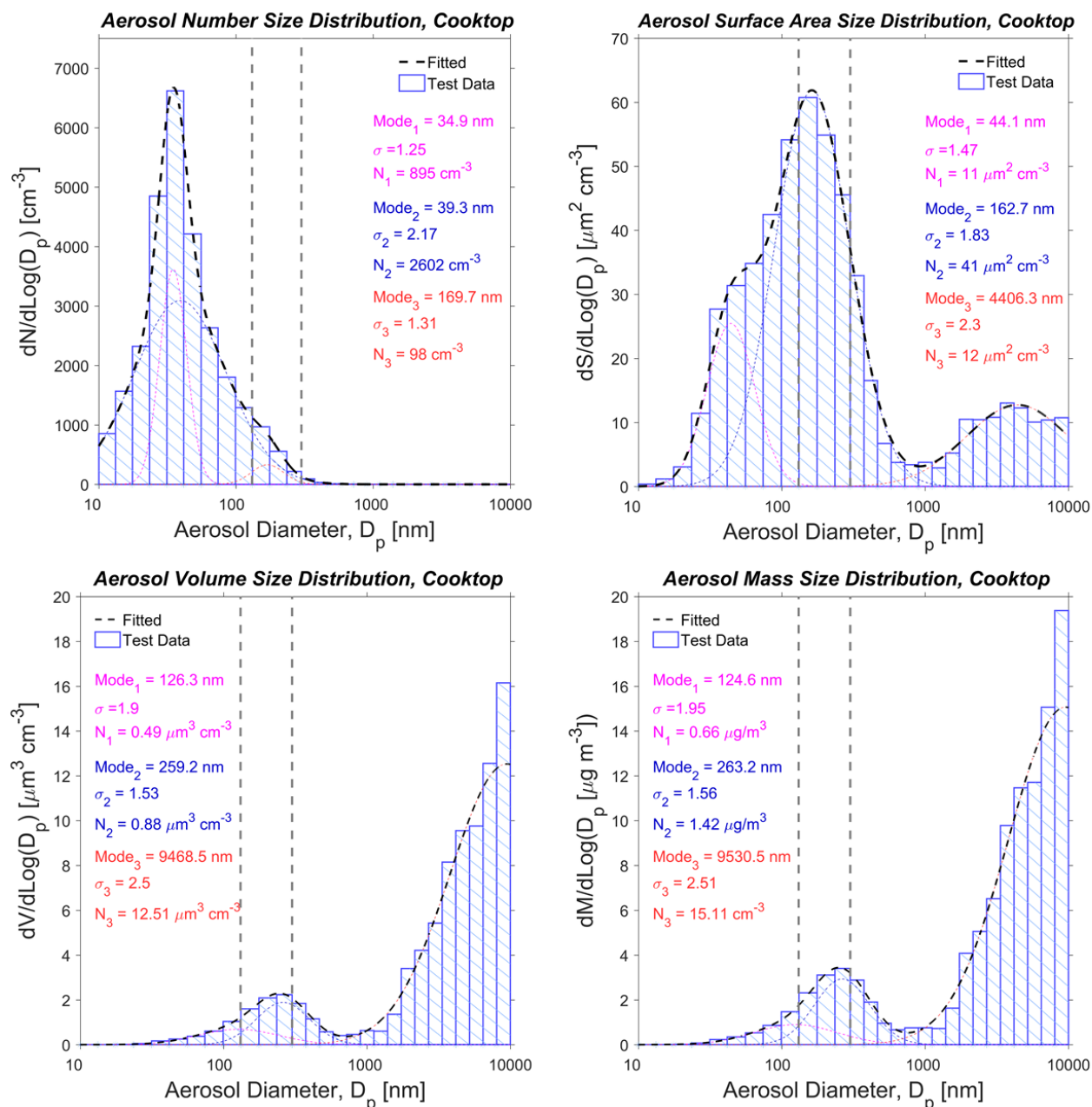


Figure 3.6 Median aerosol size distributions for the cooktop from 10 nm to 10,000 nm: (a.) aerosol number size distribution ($dN/d\log D_p$, cm^{-3}); (b.) aerosol surface area distribution ($dS/d\log D_p$, $\mu\text{m}^2 \text{ cm}^{-3}$); (c.) aerosol volume distribution ($dV/d\log D_p$, $\mu\text{m}^3 \text{ cm}^{-3}$); (d.) aerosol mass distribution ($dM/d\log D_p$, $\mu\text{g m}^{-3}$). Dashed black curves show the log-normal fitting of the measured distributions and dashed pink, blue, and red curves denote the individual modes. The geometric mean diameter ($Mode_i$), geometric standard deviation (σ_i), and amplitude (N_i , S_i , V_i , M_i) for each are presented.

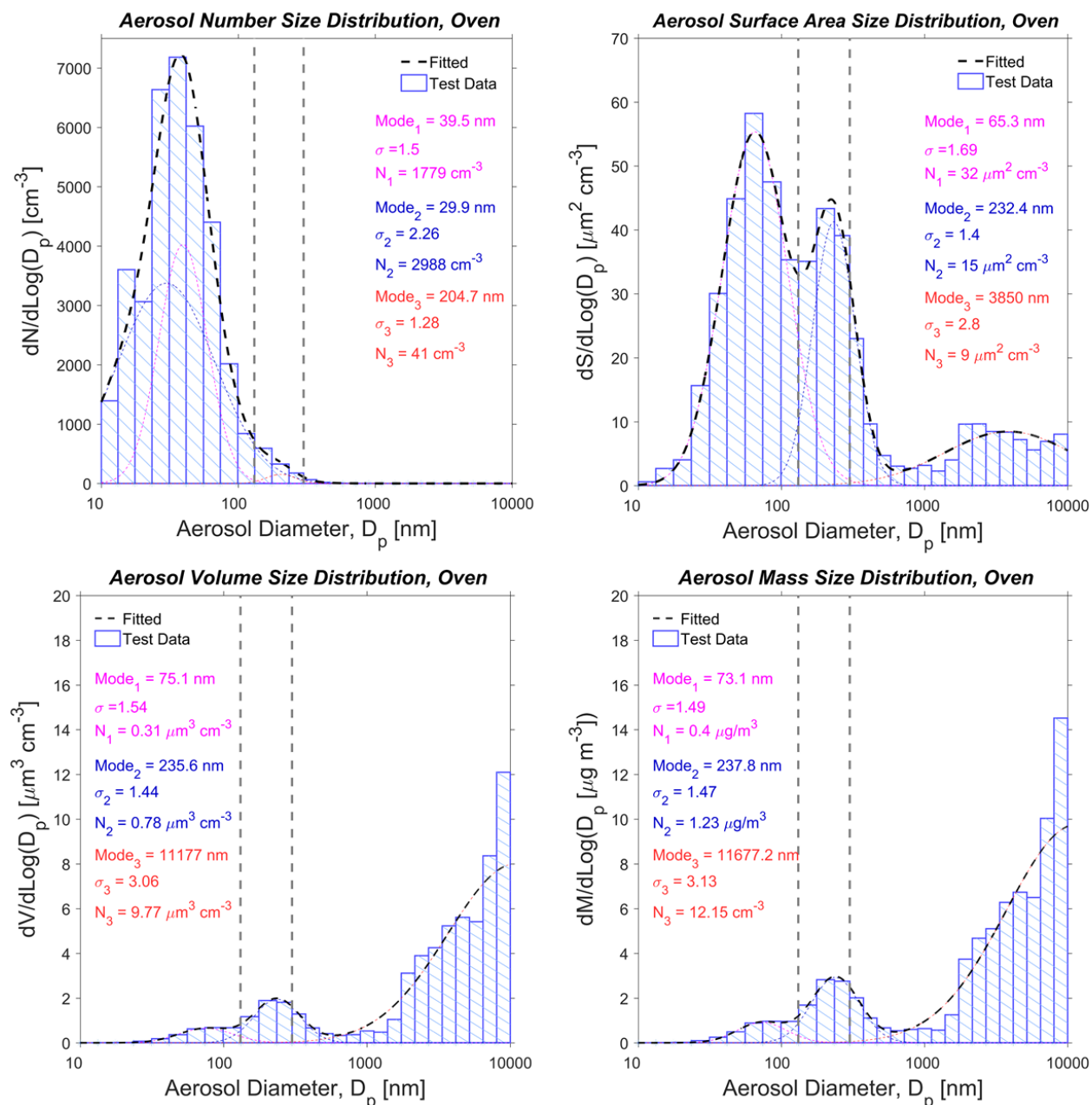


Figure 3.7 Median aerosol size distributions for the oven from 10 nm to 10,000 nm: (a.) aerosol number size distribution ($dN/d\log D_p$, cm^{-3}); (b.) aerosol surface area distribution ($dS/d\log D_p$, $\mu\text{m}^2 \text{ cm}^{-3}$); (c.) aerosol volume distribution ($dV/d\log D_p$, $\mu\text{m}^3 \text{ cm}^{-3}$); (d.) aerosol mass distribution ($dM/d\log D_p$, $\mu\text{g m}^{-3}$). Dashed black curves show the log-normal fitting of the measured distributions and dashed pink, blue, and red curves denote the individual modes. The geometric mean diameter ($Mode_i$), geometric standard deviation (σ_i), and amplitude (N_i , S_i , V_i , M_i) for each are presented.

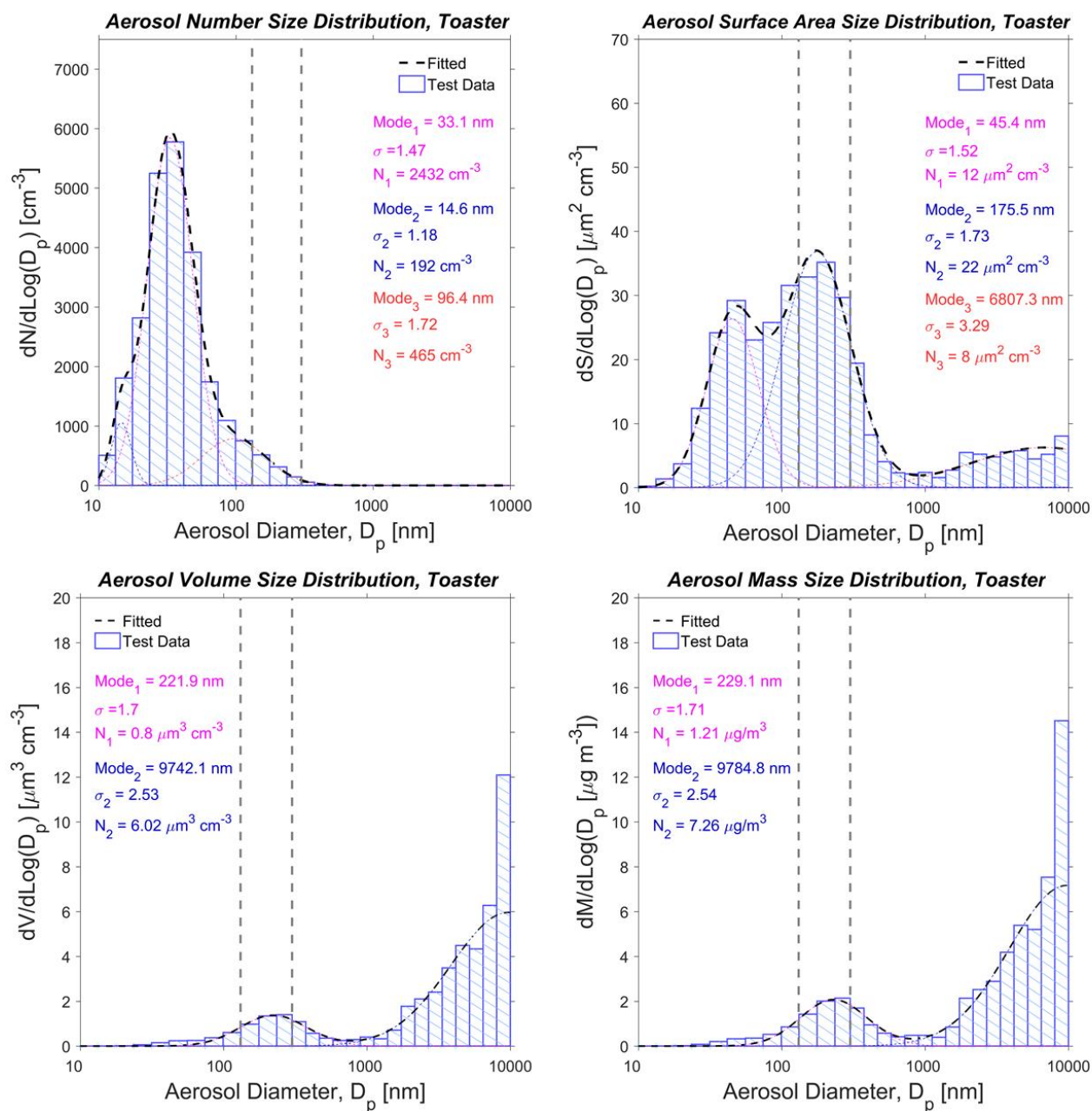


Figure 3.8 Median aerosol size distributions for the toaster from 10 nm to 10,000 nm: (a.) aerosol number size distribution ($dN/d\log D_p$, cm^{-3}); (b.) aerosol surface area distribution ($dS/d\log D_p$, $\mu\text{m}^2 \text{ cm}^{-3}$); (c.) aerosol volume distribution ($dV/d\log D_p$, $\mu\text{m}^3 \text{ cm}^{-3}$); (d.) aerosol mass distribution ($dM/d\log D_p$, $\mu\text{g m}^{-3}$). Dashed black curves show the log-normal fitting of the measured distributions and dashed pink, blue, and red curves denote the individual modes. The geometric mean diameter ($Mode_i$), geometric standard deviation (σ_i), and amplitude (N_i , S_i , V_i , M_i) for each are presented.

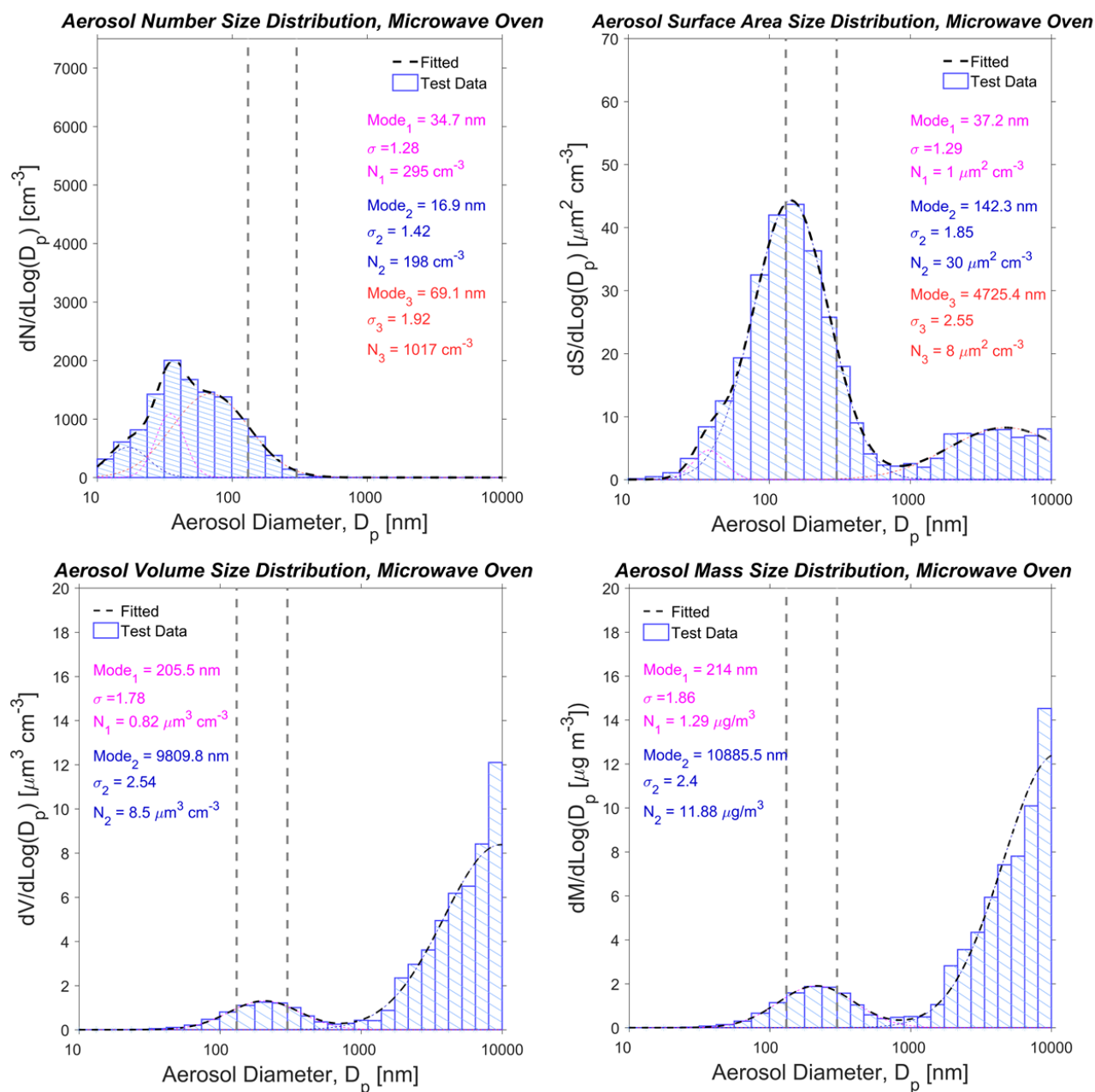


Figure 3.9 Median aerosol size distributions for the microwave oven from 10 nm to 10,000 nm: (a.) aerosol number size distribution ($dN/d\log D_p$, cm^{-3}); (b.) aerosol surface area distribution ($dS/d\log D_p$, $\mu\text{m}^2 \text{cm}^{-3}$); (c.) aerosol volume distribution ($dV/d\log D_p$, $\mu\text{m}^3 \text{cm}^{-3}$); (d.) aerosol mass distribution ($dM/d\log D_p$, $\mu\text{g m}^{-3}$). Dashed black curves show the log-normal fitting of the measured distributions and dashed pink, blue, and red curves denote the individual modes. The geometric mean diameter ($Mode_i$), geometric standard deviation (σ_i), and amplitude (N_i , S_i , V_i , M_i) for each are presented.

Table 3.2 Parameters of the indoor aerosol number, surface area, volume and mass size distributions for the four electrical kitchen appliances.

Appliance	Mode 1			Mode 2			Mode 3		
Aerosol Number Size Distributions									
	N_1 (cm^{-3})	$\overline{D_{pg,1}}$ (nm)	$\sigma_{g,1}$ (-)	N_2 (cm^{-3})	$\overline{D_{pg,2}}$ (nm)	$\sigma_{g,2}$ (-)	N_3 (cm^{-3})	$\overline{D_{pg,3}}$ (nm)	$\sigma_{g,3}$ (-)
Cooktop	895	34.9	1.25	2602	39.3	2.17	98	169.7	1.31
Oven	2988	29.9	2.26	1779	39.5	1.50	41	204.7	1.28
Toaster	192	14.6	1.18	2432	33.1	1.47	465	96.4	1.72
Microwave Oven	198	16.9	1.42	295	34.7	1.28	1017	69.1	1.92
Aerosol Surface Area Size Distributions									
	N_1 (μm^2 cm^{-3})	$\overline{D_{pg,1}}$ (nm)	$\sigma_{g,1}$ (-)	N_2 (μm^2 cm^{-3})	$\overline{D_{pg,2}}$ (nm)	$\sigma_{g,2}$ (-)	N_3 (μm^2 cm^{-3})	$\overline{D_{pg,3}}$ (nm)	$\sigma_{g,3}$ (-)
Cooktop	11	44.1	1.47	41	162.7	1.83	12	4406.3	2.30
Oven	32	65.3	1.69	15	232.4	1.40	9	3850.0	2.80
Toaster	12	45.4	1.52	22	175.5	1.73	8	6807.3	3.29
Microwave Oven	1	37.2	1.29	30	142.3	1.85	8	4725.4	2.55
Aerosol Volume Size Distributions									
	N_1 (μm^3 cm^{-3})	$\overline{D_{pg,1}}$ (nm)	$\sigma_{g,1}$ (-)	N_2 (μm^3 cm^{-3})	$\overline{D_{pg,2}}$ (nm)	$\sigma_{g,2}$ (-)	N_3 (μm^3 cm^{-3})	$\overline{D_{pg,3}}$ (nm)	$\sigma_{g,3}$ (-)
Cooktop	0.49	126.3	1.90	0.88	259.2	1.53	12.51	9468.5	2.50
Oven	0.31	75.1	1.54	0.78	235.6	1.44	9.77	11177	3.06
Toaster	0.8	221.9	1.7	6.02	9742.1	2.53	-	-	-
Microwave Oven	0.82	205.5	1.78	8.5	9808.8	2.54	-	-	-
Aerosol Mass Size Distributions									
	N_1 (μg cm^{-3})	$\overline{D_{pg,1}}$ (nm)	$\sigma_{g,1}$ (-)	N_2 (μg cm^{-3})	$\overline{D_{pg,2}}$ (nm)	$\sigma_{g,2}$ (-)	N_3 (μg cm^{-3})	$\overline{D_{pg,3}}$ (nm)	$\sigma_{g,3}$ (-)
Cooktop	0.66	124.6	1.95	1.42	263.2	1.56	15.11	9530.5	2.51
Oven	0.4	73.1	1.49	1.23	237.8	1.47	12.15	11677.2	3.13
Toaster	1.21	229.1	1.71	7.26	9784.8	2.54	-	-	-
Microwave Oven	1.29	214	1.86	11.88	10885.5	2.4	-	-	-

During different periods of the day, different types of indoor activities dominate. The aerosol size distributions through the campaign were divided into five groups based on the density of activities in different time periods. From Figure 3.10, it can be observed that the magnitude of $dN/d\log D_p$ is the greatest from 17:00 to 23:00, when most cooking activities occurred. The second greatest distribution occurred from 12:00 to 14:00, during which many cooking activities happened on weekdays. From 14:00 to 17:00, cooking activities more sporadically, but not to the extent of that which occurred at noon and in the evening, resulting in a $dN/d\log D_p$ with a lower magnitude. From 23:00 to 07:00, residents were asleep, there were no active emission sources, and the outdoor aerosol concentration remained low. Thus, the indoor aerosol concentration decayed, leading to a size distribution with a lower magnitude. From 07:00 to 12:00 in the morning, the aerosol concentration dropped to a steady-state, and few cooking events occurred during this period, so $dN/d\log D_p$ was at the lowest magnitude among all time periods. Figures 3.11-3.15 shows the aerosol number, surface area, volume and mass size distribution for each time period.

The parameters of the size distributions are summarized in Table 3.3. Indoor aerosol number size distributions during different time periods can be bi-modal or tri-modal. The Aitken mode between 30 nm – 50 nm dominates the distribution for all time periods. However, the contribution of Aitken mode is much more significant during 12:00 – 14:00 and 17:00 – 23:00 than in other time periods, with the number concentration at 1780 cm^{-3} and 1678 cm^{-3} in the dominant mode, respectively. The surface area size distributions are tri-modal, with three modes at Aitken mode, accumulation mode and coarse mode, respectively. There is no significant difference between the surface area distributions of 23:00 – 07:00 and 07:00 – 12:00. The GMDs of the coarse mode during 23:00 – 07:00 and 07:00 – 12:00 are at 1911.9 nm and 1919.7 nm, respectively, which are smaller than other time periods. Similarly, the volume and mass distributions during these two periods also have a smaller GMD in coarse mode. There were not many indoor activities during midnight and morning as in the afternoon and evening, so there would be less larger aerosols resuspended from the floor through the movements of occupants.

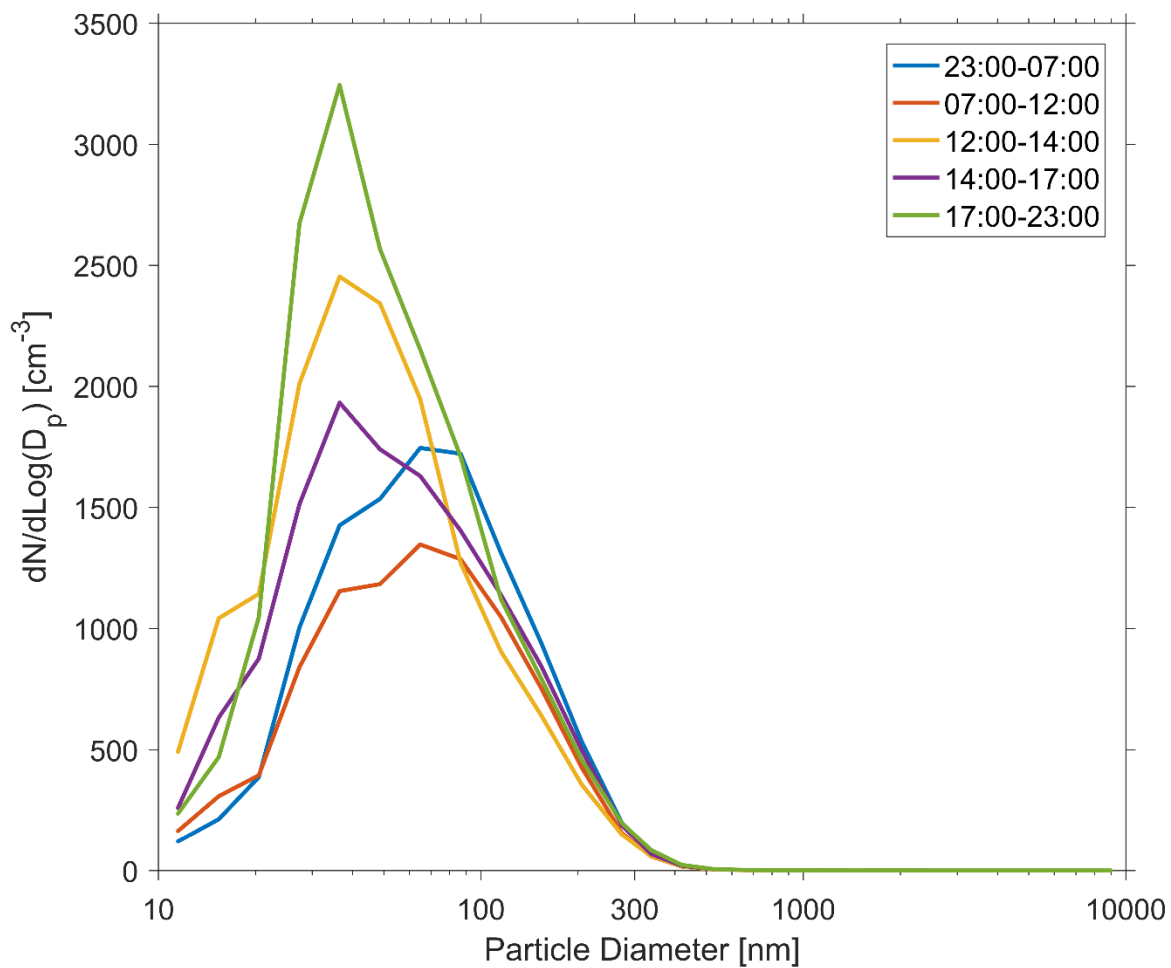


Figure 3.10 Median indoor aerosol number size distributions ($dN/d\log D_p$, cm^{-3}) from 10 nm to 10,000 nm for different periods of the day.

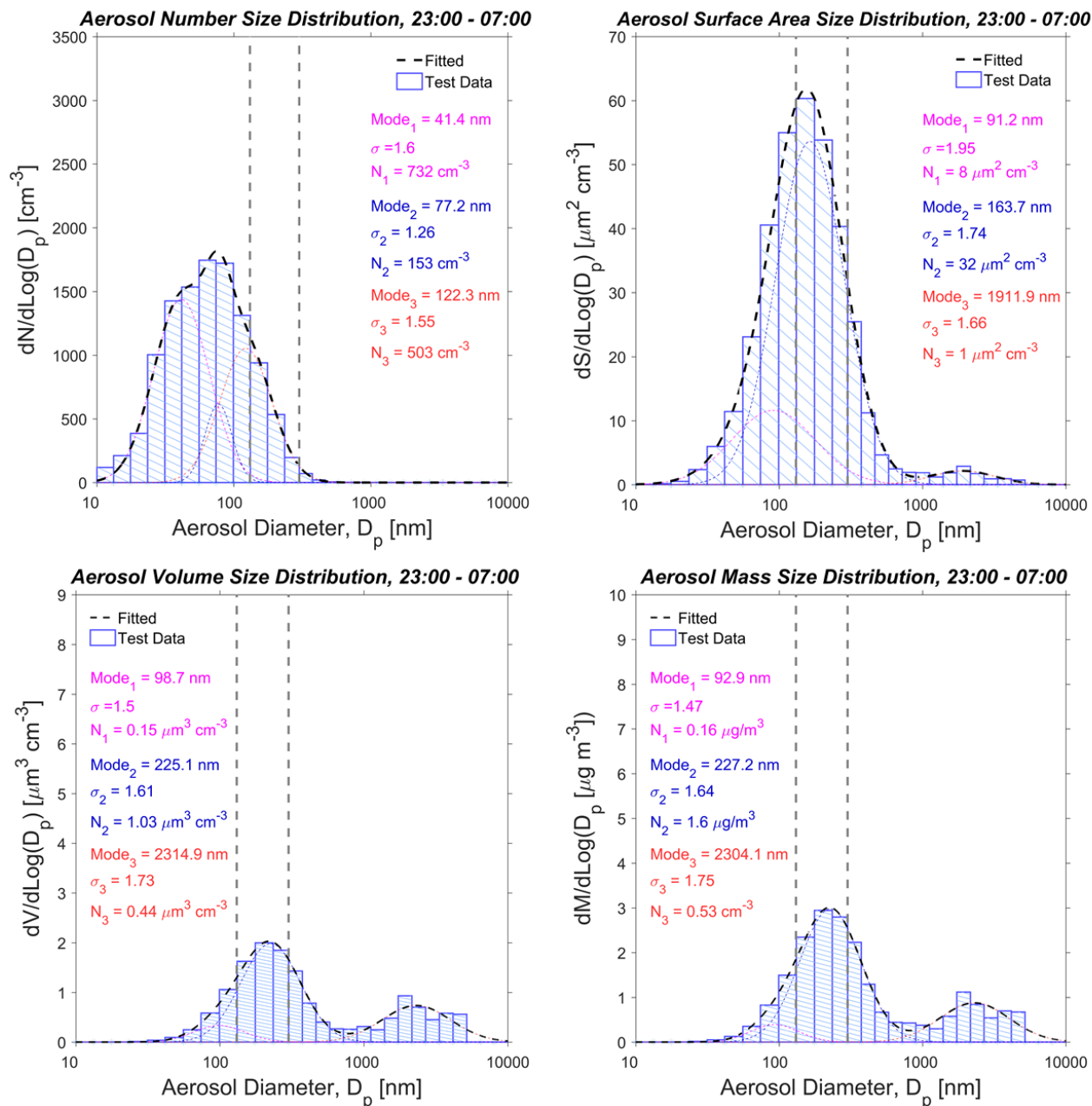


Figure 3.11 Median aerosol size distributions during 23:00 to 7:00 from 10 nm to 10,000 nm: (a.) aerosol number size distribution ($dN/d\log D_p$, cm^{-3}); (b.) aerosol surface area distribution ($dS/d\log D_p$, $\mu\text{m}^2 \text{ cm}^{-3}$); (c.) aerosol volume distribution ($dV/d\log D_p$, $\mu\text{m}^3 \text{ cm}^{-3}$); (d.) aerosol mass distribution ($dM/d\log D_p$, $\mu\text{g m}^{-3}$). Dashed black curves show the log-normal fitting of the measured distributions and dashed pink, blue, and red curves denote the individual modes. The geometric mean diameter ($Mode_i$), geometric standard deviation (σ_i), and amplitude (N_i , S_i , V_i , M_i) for each are presented.

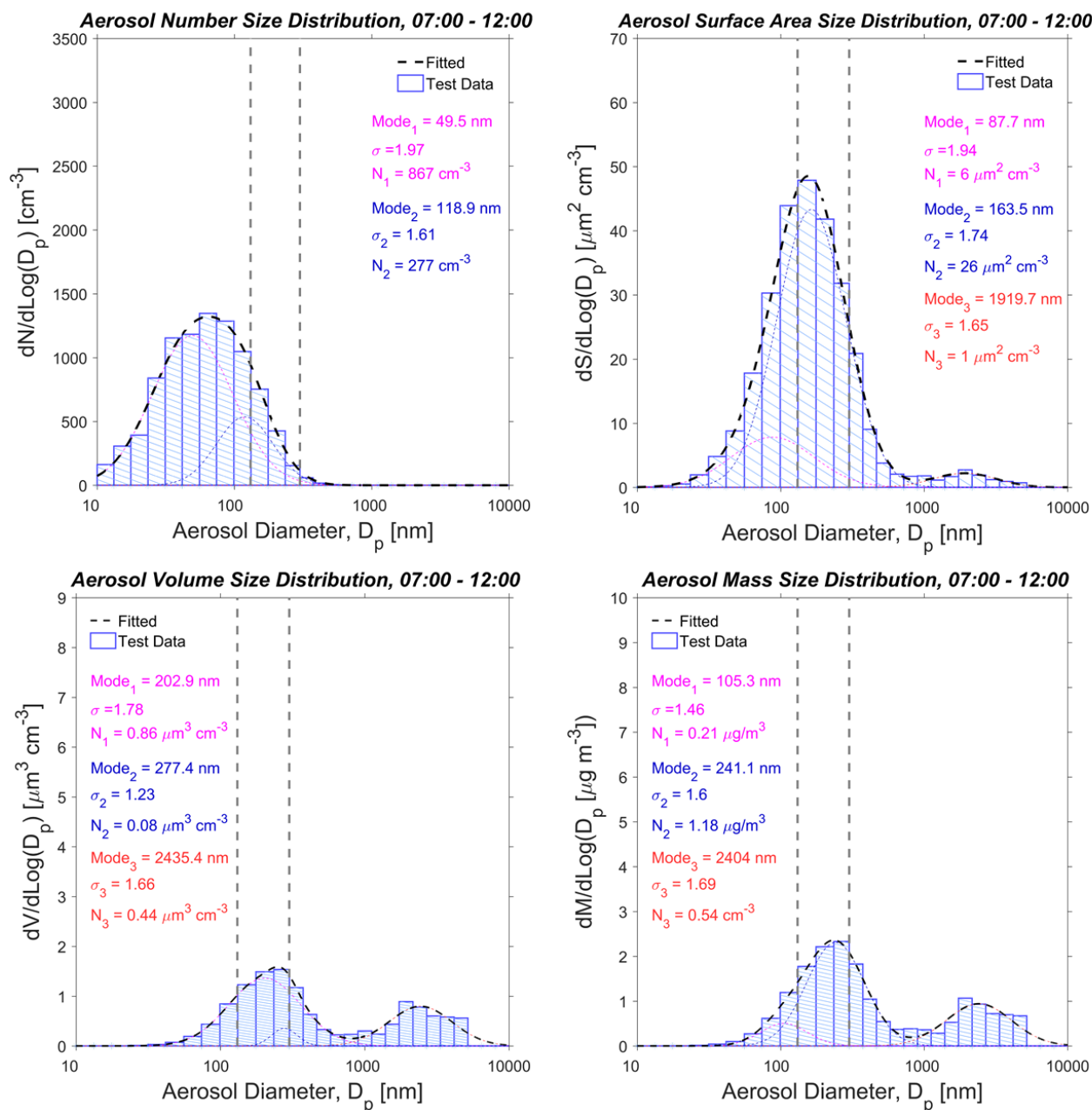


Figure 3.12 Median aerosol size distributions during 07:00 to 12:00 from 10 nm to 10,000 nm: (a.) aerosol number size distribution ($dN/d\log D_p$, cm^{-3}); (b.) aerosol surface area distribution ($dS/d\log D_p$, $\mu\text{m}^2 \text{ cm}^{-3}$); (c.) aerosol volume distribution ($dV/d\log D_p$, $\mu\text{m}^3 \text{ cm}^{-3}$); (d.) aerosol mass distribution ($dM/d\log D_p$, $\mu\text{g m}^{-3}$). Dashed black curves show the log-normal fitting of the measured distributions and dashed pink, blue, and red curves denote the individual modes. The geometric mean diameter ($Mode_i$), geometric standard deviation (σ_i), and amplitude (N_i , S_i , V_i , M_i) for each are presented.

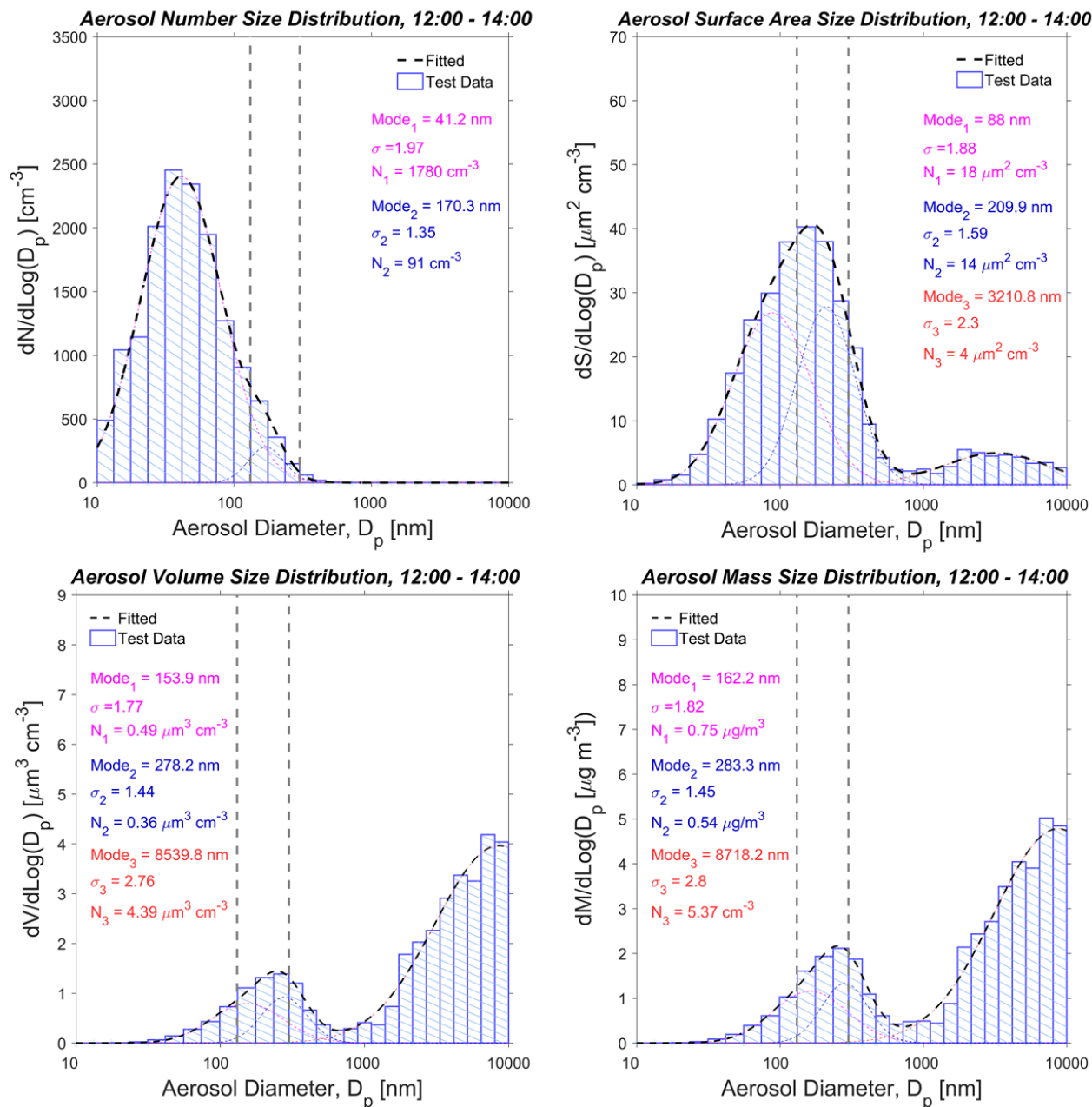


Figure 3.13 Median aerosol size distributions during 12:00 to 14:00 from 10 nm to 10,000 nm: (a.) aerosol number size distribution ($dN/d\log D_p$, cm^{-3}); (b.) aerosol surface area distribution ($dS/d\log D_p$, $\mu\text{m}^2 \text{ cm}^{-3}$); (c.) aerosol volume distribution ($dV/d\log D_p$, $\mu\text{m}^3 \text{ cm}^{-3}$); (d.) aerosol mass distribution ($dM/d\log D_p$, $\mu\text{g m}^{-3}$). Dashed black curves show the log-normal fitting of the measured distributions and dashed pink, blue, and red curves denote the individual modes. The geometric mean diameter ($Mode_i$), geometric standard deviation (σ_i), and amplitude (N_i , S_i , V_i , M_i) for each are presented.

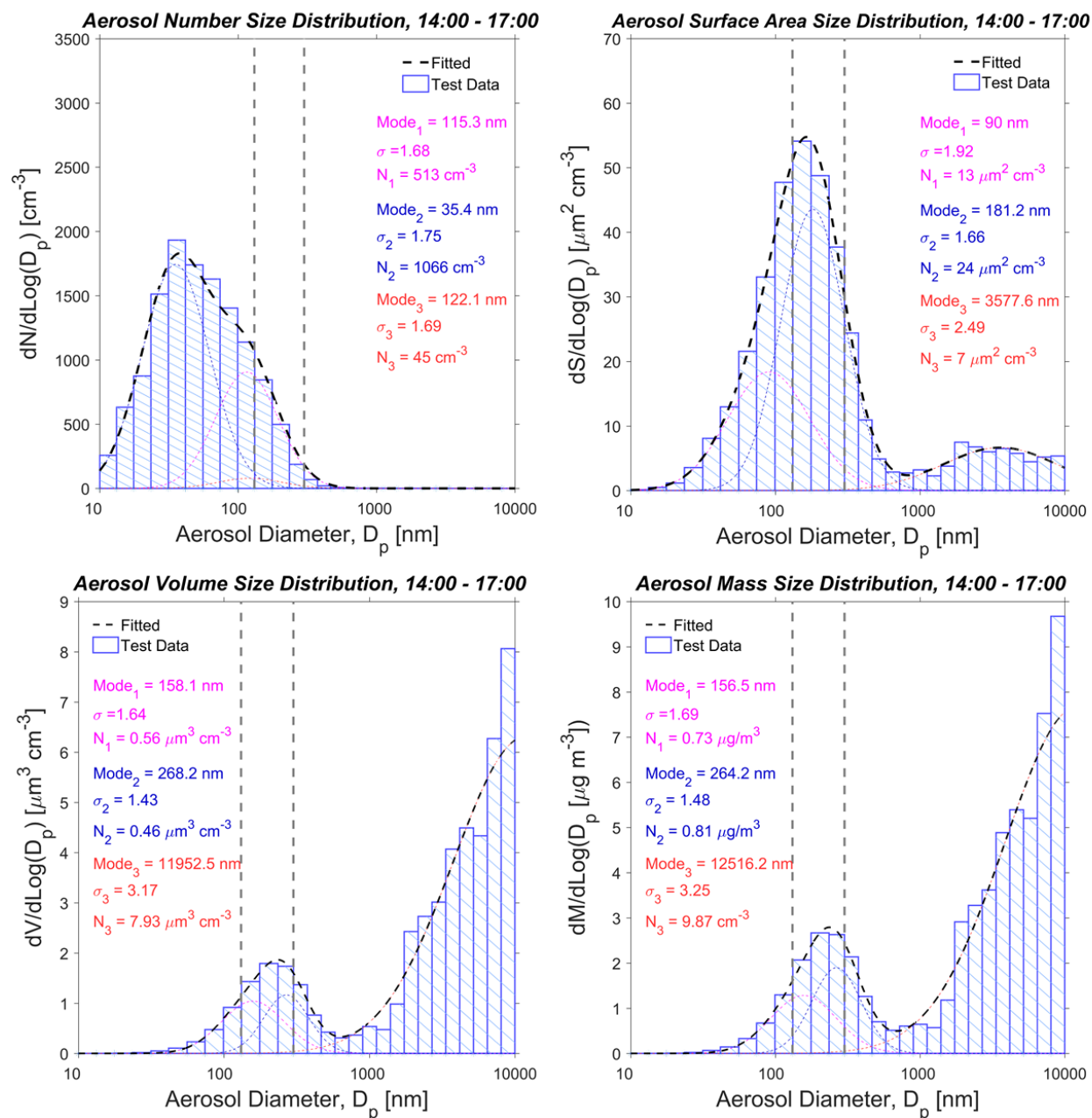


Figure 3.14 Median aerosol size distributions during 14:00 to 17:00 from 10 nm to 10,000 nm: (a.) aerosol number size distribution ($dN/d\log D_p$, cm^{-3}); (b.) aerosol surface area distribution ($dS/d\log D_p$, $\mu\text{m}^2 \text{ cm}^{-3}$); (c.) aerosol volume distribution ($dV/d\log D_p$, $\mu\text{m}^3 \text{ cm}^{-3}$); (d.) aerosol mass distribution ($dM/d\log D_p$, $\mu\text{g m}^{-3}$). Dashed black curves show the log-normal fitting of the measured distributions and dashed pink, blue, and red curves denote the individual modes. The geometric mean diameter ($Mode_i$), geometric standard deviation (σ_i), and amplitude (N_i , S_i , V_i , M_i) for each are presented.

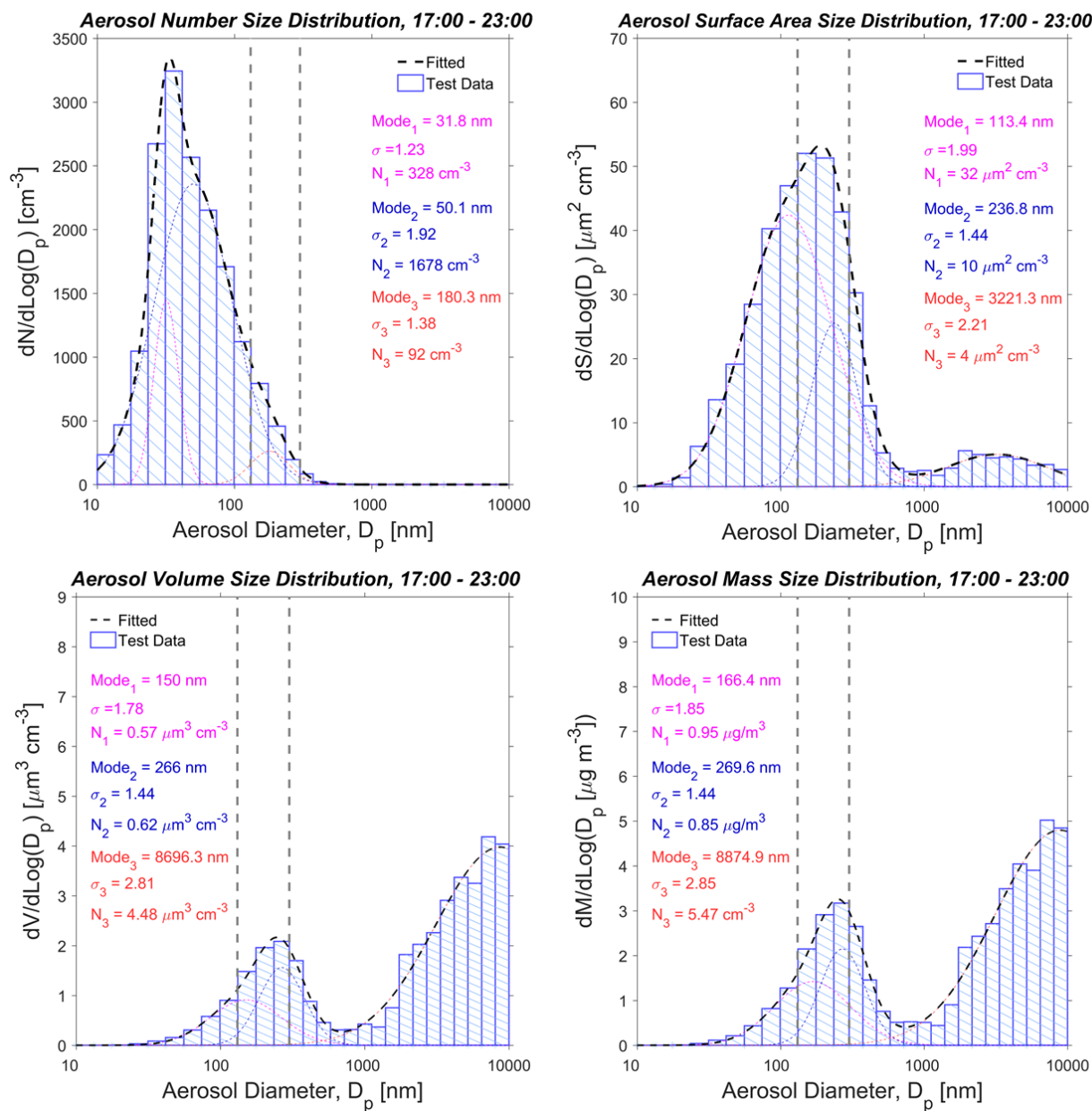


Figure 3.15 Median aerosol size distributions during 17:00 to 23:00 from 10 nm to 10,000 nm: (a.) aerosol number size distribution ($dN/d\log D_p$, cm^{-3}); (b.) aerosol surface area distribution ($dS/d\log D_p$, $\mu\text{m}^2 \text{ cm}^{-3}$); (c.) aerosol volume distribution ($dV/d\log D_p$, $\mu\text{m}^3 \text{ cm}^{-3}$); (d.) aerosol mass distribution ($dM/d\log D_p$, $\mu\text{g} \text{ m}^{-3}$). Dashed black curves show the log-normal fitting of the measured distributions and dashed pink, blue, and red curves denote the individual modes. The geometric mean diameter ($Mode_i$), geometric standard deviation (σ_i), and amplitude (N_i , S_i , V_i , M_i) for each are presented.

Table 3.3 Parameters of the indoor aerosol number, surface area, volume and mass size distributions for different periods of the day.

Time Period	Mode1			Mode2			Mode3		
Aerosol Number Size Distributions									
	N_1 (cm^{-3})	$\overline{D_{pg,1}}$ (nm)	$\sigma_{g,1}$ (-)	N_2 (cm^{-3})	$\overline{D_{pg,2}}$ (nm)	$\sigma_{g,2}$ (-)	N_3 (cm^{-3})	$\overline{D_{pg,3}}$ (nm)	$\sigma_{g,3}$ (-)
23:00 – 07:00	732	41.4	1.60	153	77.2	1.26	503	122.3	1.55
07:00 – 12:00	867	49.5	1.97	277	118.9	1.61	-	-	-
12:00 – 14:00	1780	41.2	1.97	91	170.3	1.35	-	-	-
14:00 – 17:00	513	115.3	1.68	1066	35.4	1.75	45	122.1	1.69
17:00 – 23:00	328	31.8	1.23	1678	50.1	1.92	92	180.3	1.38
Aerosol Surface Area Size Distributions									
	N_1 (μm^2 cm^{-3})	$\overline{D_{pg,1}}$ (nm)	$\sigma_{g,1}$ (-)	N_2 (μm^2 cm^{-3})	$\overline{D_{pg,2}}$ (nm)	$\sigma_{g,2}$ (-)	N_3 (μm^2 cm^{-3})	$\overline{D_{pg,3}}$ (nm)	$\sigma_{g,3}$ (-)
23:00 – 07:00	8	91.2	1.95	32	163.7	1.74	1	1911.9	1.66
07:00 – 12:00	6	87.7	1.94	26	163.5	1.74	1	1919.7	1.65
12:00 – 14:00	18	88	1.88	14	209.9	1.59	4	3210.8	2.3
14:00 – 17:00	13	90	1.92	24	181.2	1.66	7	3577.6	2.49
17:00 – 23:00	32	113.4	1.99	10	236.8	1.44	4	3221.3	2.21
Aerosol Surface Area Size Distributions									
	N_1 (μm^3 cm^{-3})	$\overline{D_{pg,1}}$ (nm)	$\sigma_{g,1}$ (-)	N_2 (μm^3 cm^{-3})	$\overline{D_{pg,2}}$ (nm)	$\sigma_{g,2}$ (-)	N_3 (μm^3 cm^{-3})	$\overline{D_{pg,3}}$ (nm)	$\sigma_{g,3}$ (-)
23:00 – 07:00	0.15	98.7	1.5	1.03	225.1	1.61	0.44	2314.9	1.73
07:00 – 12:00	0.86	202.9	1.78	0.08	277.4	1.23	0.44	2435.4	1.66
12:00 – 14:00	0.49	153.9	1.77	278.2	0.36	1.44	4.39	8539.8	2.76
14:00 – 17:00	0.56	158.1	1.64	0.46	268.2	1.43	7.93	11952.5	3.17
17:00 – 23:00	0.57	150	1.78	0.62	266	1.44	4.48	8698.3	2.81
Aerosol Surface Area Size Distributions									
	N_1 (μg cm^{-3})	$\overline{D_{pg,1}}$ (nm)	$\sigma_{g,1}$ (-)	N_2 (μg cm^{-3})	$\overline{D_{pg,2}}$ (nm)	$\sigma_{g,2}$ (-)	N_3 (μg cm^{-3})	$\overline{D_{pg,3}}$ (nm)	$\sigma_{g,3}$ (-)
23:00 – 07:00	0.16	92.9	1.47	1.6	227.2	1.64	0.53	2304.1	1.75
07:00 – 12:00	0.21	105.3	1.46	1.18	241.1	1.60	0.54	2404.0	1.69
12:00 – 14:00	0.75	162.2	0.75	0.54	283.3	1.45	5.37	8718.2	2.80
14:00 – 17:00	0.73	156.5	1.69	0.81	264.2	1.48	9.87	12516.2	3.25
17:00 – 23:00	0.95	166.4	1.85	0.85	269.6	1.44	5.47	8874.9	2.85

3.2 HVAC system run-time

As both the AHU and ERV can serve as a source and loss of nanoaerosols in the ReNEWW House, it is important to characterize the run-time of each HVAC component via energy monitoring data. Figure 3.16 shows the variation of AHU and ERV power consumption throughout the one-month field campaign. The AHU/ERV off and on status are indicated by the colorbar (e.g. blue = off, green-red = on). It can be seen that the ERV follows a preset cycle during the observational period, except for some interferences. The AHU was active less frequently during the latter stages of the campaign, due to the increase of outdoor temperature, and thus less demand for heating.

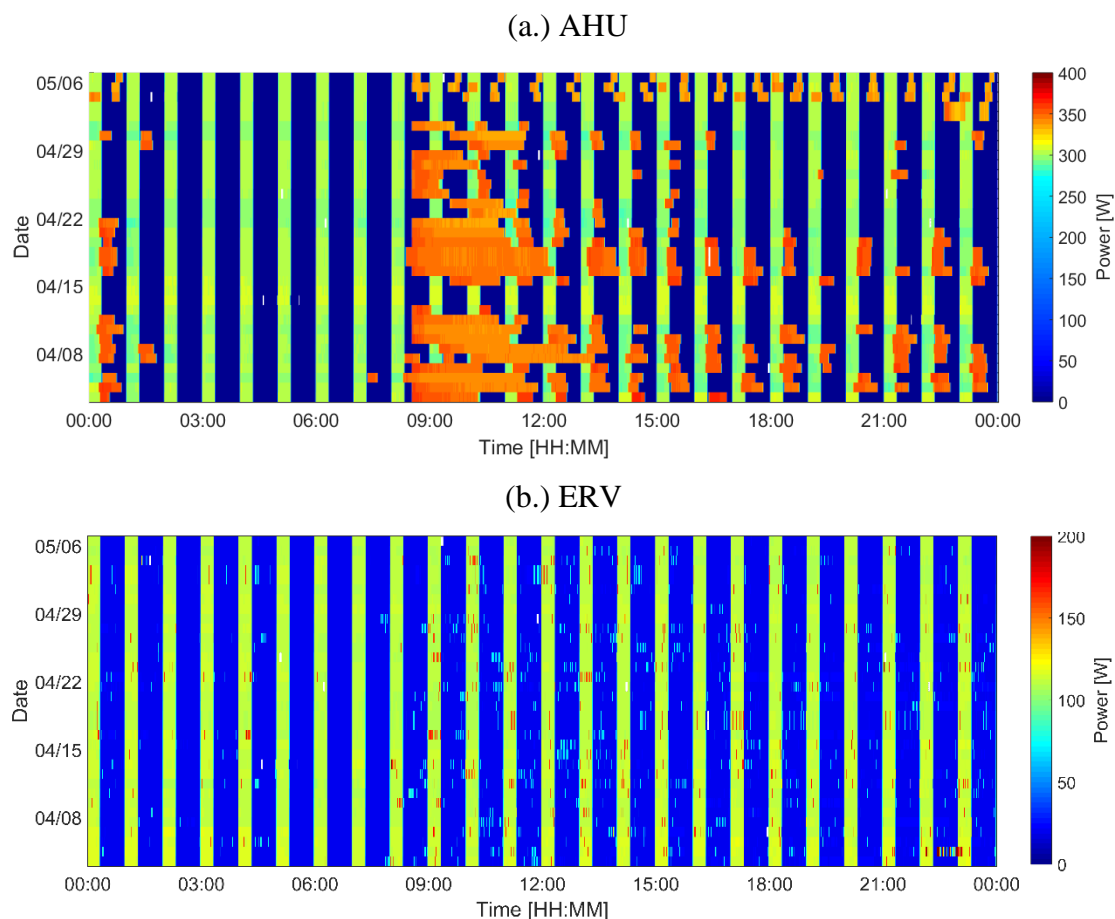


Figure 3.16 Temporal power usage profiles of the ReNEWW House AHU and ERV from April 03, 2018 to May 06, 2018. Colorbar indicates power consumption in W.

Figure 3.17 demonstrates that the AHU runtime was the highest in the morning, reaching 74% at around 10:00. It was the lowest in the early morning from 02:00 to 07:00, at around 36%, indicating that the ERV was on and there was no calling for heating. The ERV runtime was

maintained at approximately 36% throughout the day. Thus, outdoor nanoaerosols will only be delivered into the occupied space via forced mechanical ventilation during these periods. Compared to previous investigations, the median AHU run-time at ReNEWW House (36.7%) is within the range of the median HVAC system run-times in heating-dominated climates and during a heating season (35% - 45%), and longer than the run-times in cooling dominated climates (20% - 27%) (Touchie and Siegel 2018).

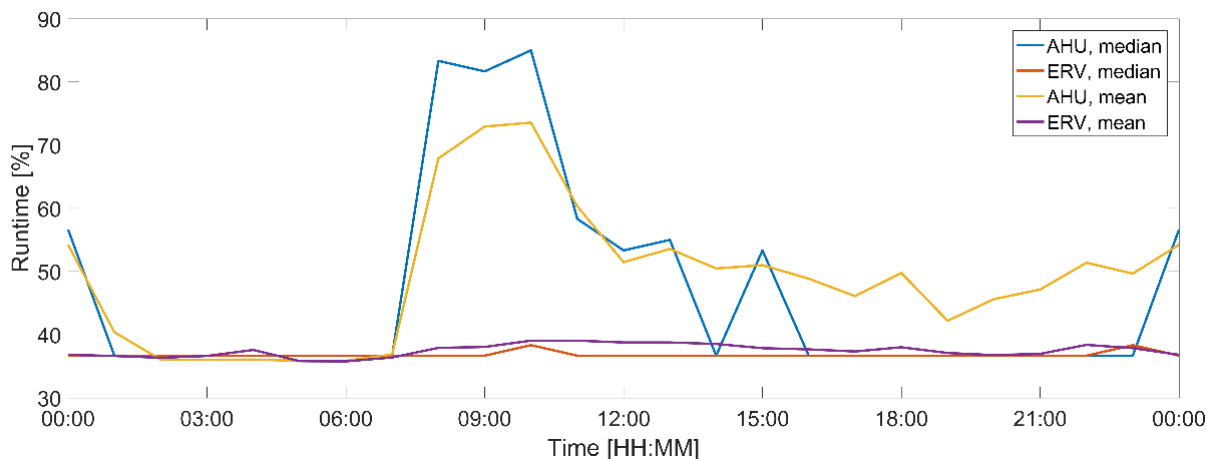


Figure 3.17 Median and mean diurnal run-time profile of the ReNEWW House AHU and ERV.

3.3 Nanoaerosol loss rates

The decay periods following an indoor emission event when indoor nanoaerosol concentration removed greater than $1.5 \times 10^3 \text{ cm}^{-3}$ were selected for the estimation of size-integrated loss rates (10 nm to 100 nm). The table below summarizes the number of decay periods that occurred under each HVAC system operational status, as indicated by the energy monitoring and smart thermostat data. Considering there was limited data for the “AHU on, ERV on, main floor heating on” condition compared to the other modes, the “AHU on, ERV on, main floor heating off” and “AHU on, ERV on, main floor heating on” were merged into a single group, “AHU on, ERV on” for further analysis.

Table 3.4 Number of loss rates calculated for each HVAC system operational condition.

HVAC system status	Number of occurrences
AHU off, ERV off	13
AHU on, ERV off	14
AHU on, ERV on, main floor heating off	22
AHU on, ERV on, main floor heating on	7

Kernel density functions of the size-integrated nanoaerosol loss rates under the three HVAC operational conditions are presented in Figure 3.18. There are notable differences in the loss rates among the three HVAC system operational conditions. Overall, the loss rates when both the AHU and ERV were on were the largest, followed by AHU on, ERV off. When both the AHU and ERV were off, the loss rates were the lowest, with a median value at 1.43 h^{-1} , and the distribution of the loss rates were much more uniform than the other scenarios. Although the curve shows that the loss rate probability for the AHU on, ERV off condition was the greatest at approximately 2.0 h^{-1} , the variation of loss rates in this case was very large, with the highest loss rate reaching 8.0 h^{-1} . Similarly, the loss rates when both the AHU and ERV were on were also quite variable. The median values of the two HVAC systems modes are close to each other, with 3.54 h^{-1} for AHU on, ERV off and 3.70 h^{-1} for AHU on, ERV on, respectively.

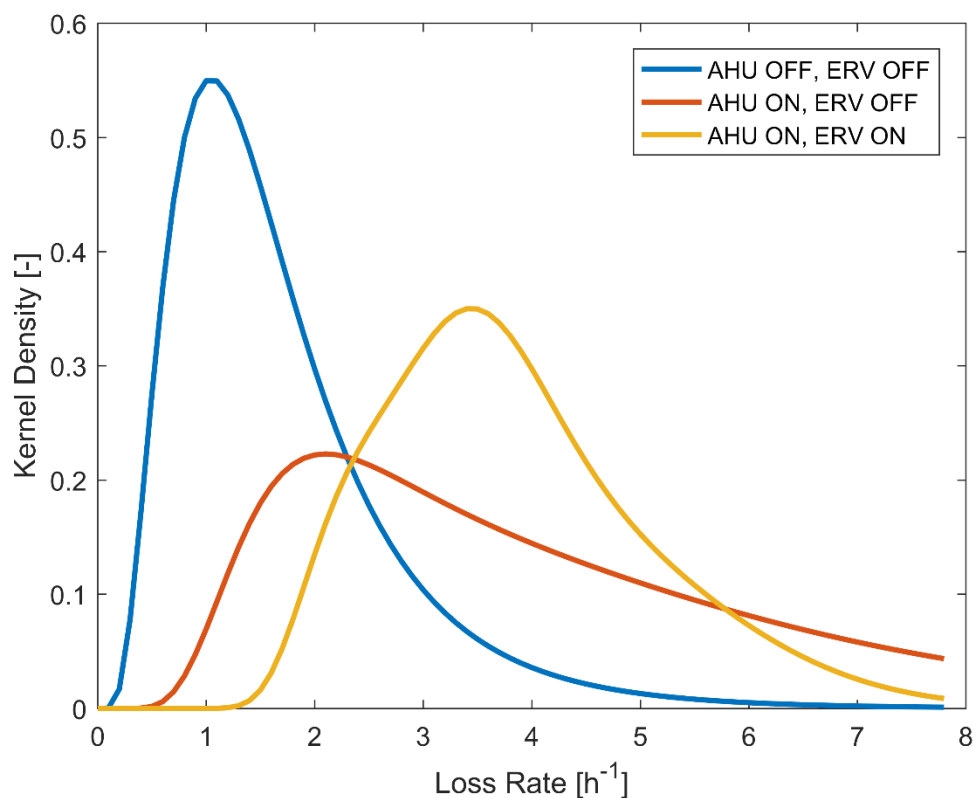


Figure 3.18 Kernel density functions of size-integrated nanoaerosol loss rates (h^{-1}) under three HVAC system operational conditions.

3.4 Nanoaerosol source rates

Figure 3.19 shows the size-integrated (10 nm to 100 nm) nanoaerosol source rates (h^{-1}) under different HVAC system operational conditions and the source (emission) rates (h^{-1}) of each kitchen appliance. The microwave oven is excluded from the emission rate analysis because there was no significant increase in nanoaerosol number concentrations when appliance was active. Overall, the emission rates for the cooktop were the highest, with a median value at $3.13 \times 10^{13} \text{ h}^{-1}$, but the variation of which was also higher due to the variety of cooking styles and food that may have been prepared with the cooktop. The emission rates of the toaster and oven were similar to each other, with median values of $1.07 \times 10^{13} \text{ h}^{-1}$ and $7.55 \times 10^{12} \text{ h}^{-1}$, respectively. The estimated emission rates for cooking agree well with the emission rates reported in previous studies (Hussein et al. 2006; Wallace et al. 2008). The variation in emission rates for toaster was lower because of the food type was likely more consistent. Although the emission rate for the oven was lower than for the cooktop, the oven was typically used for a longer periods than the cooktop. Thus, it has the potential to elevate indoor nanoaerosol concentrations beyond what the cooktop produces, as shown in Figures 3.4 and 3.5.

Compared to the emission rates from cooking on the electrical kitchen appliances, source rates for the HVAC system were lower by one to two orders of magnitude. The kernel density function of the size-integrated nanoaerosol source rates are shown in Figure 3.20. As the source rates of AHU on, ERV on, main floor heating on and AHU on, ERV off, main floor heating off were similar, these two modes were merged together. Similar to Figure 3.19, the emission rates for cooktop has more potential to be greater than the oven and toaster. The source rate probability for the HVAC

system when the ERV is on and off are the highest at source rates of $1.0 \times 10^{11} \text{ h}^{-1}$ and $1.5 \times 10^{11} \text{ h}^{-1}$, respectively.

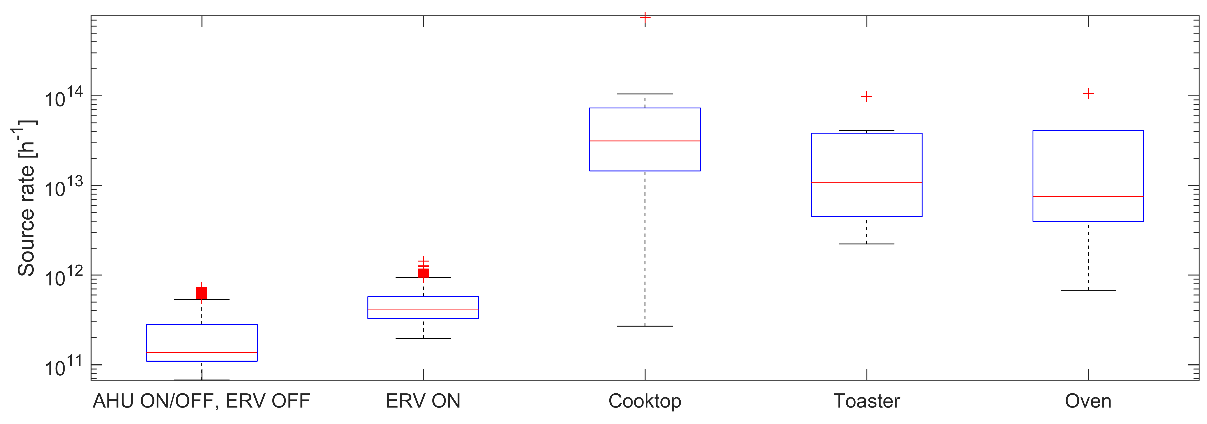


Figure 3.19 Size-integrated nanoaerosol source rates for the HVAC system under different operational conditions and each electrical kitchen appliance.

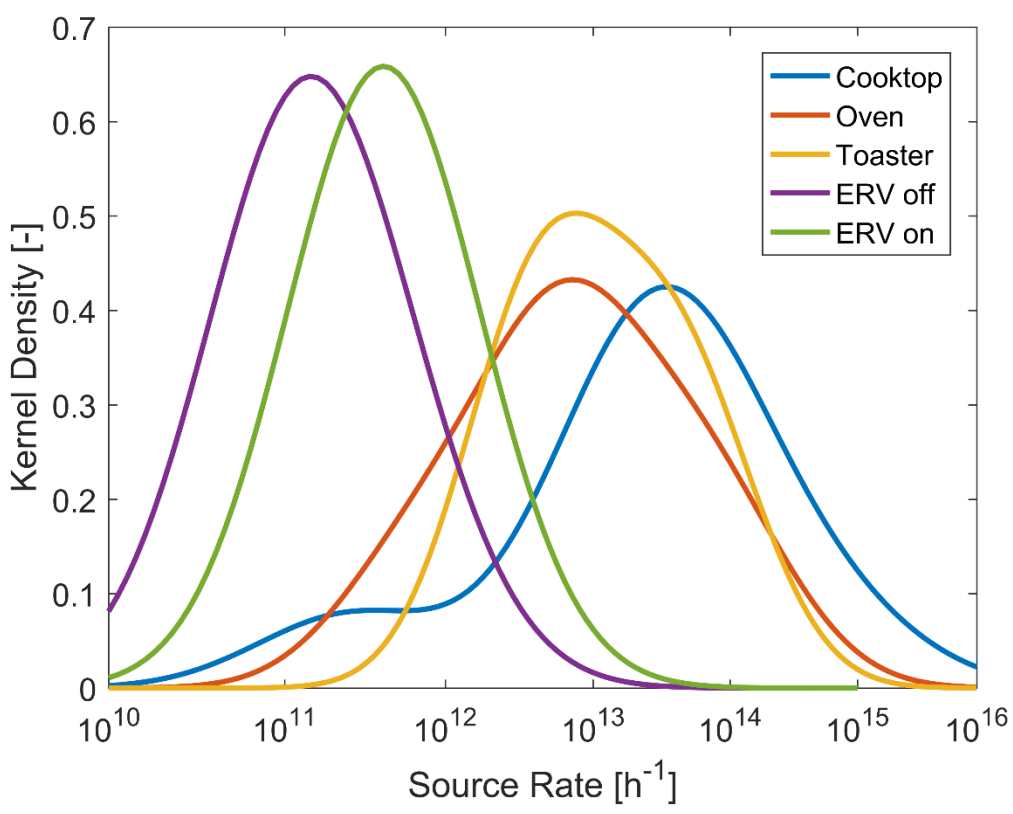


Figure 3.20 Kernel density functions of size-integrated nanoaerosol source rates (h⁻¹) for the HVAC system under different operational conditions and each electrical kitchen appliance.

4. CONCLUSIONS

This study demonstrated that energy use patterns, coupled with smart thermostat data, can provide an improved understanding of indoor nanoaerosol dynamics in a residential NZEB. Energy monitoring and smart thermostat data was integrated with an aerosol physics-based material balance model to characterize source and loss mechanisms for indoor nanoaerosols. Throughout the one-month field campaign at the Purdue ReNEW House, cooking activities were found to dominate indoor nanoaerosol emissions and contribute significantly to indoor nanoaerosol concentrations and size distributions. Compared to periods when there were no active indoor emissions, indoor nanoaerosol number concentrations during cooking events were one order of magnitude higher. Among the four cooking appliances used most frequently during the measurement period, indoor nanoaerosol concentrations when using oven was the highest, with a median value at $6.4 \times 10^3 \text{ cm}^{-3}$, followed by the cooktop and toaster. The concentration when using the microwave oven was the lowest, close to when there were no emissions, at around 10^3 cm^{-3} .

From the energy monitoring and smart thermostat data, we extracted 86 cooking periods and determined the HVAC system operational conditions for each cooking period. Loss rates were estimated for each HVAC system status. The loss rates when AHU and ERV were both on were 2.5-fold greater on average than that of AHU off, ERV off condition, indicating that the HVAC system can contribute substantially to indoor nanoaerosol loss processes. Nanoaerosol source rates were estimated for different HVAC system modes, as well as cooking on different electrical kitchen appliances. Overall, source rates for the cooking appliances were about one to two orders of magnitude greater than source rates related to the HVAC system and building envelope. Among the four cooking appliances, the emissions from microwave oven were negligible across the measured nanoaerosol size range of 10 nm to 100 nm. Emission rates for the cooktop were the highest, followed by the toaster and oven.

Future work will focus on predicting indoor nanoaerosol concentrations with the application of energy monitoring and smart thermostat data. Based on the kernel density functions of the nanoaerosol source and loss rates for different scenarios, indoor nanoaerosol concentrations will be predicted through Monte Carlo simulations, using only energy and thermostat data.

REFERENCES

- Arghira, Nicoleta, Lamis Hawarah, Stéphane Ploix, and Mireille Jacomino. 2012. "Prediction of Appliances Energy Use in Smart Homes." *Energy* 48(1):128–34.
- Ascione, Fabrizio, Nicola Bianco, Olaf Böttcher, Robert Kaltenbrunner, and Giuseppe Peter Vanoli. 2016. "Net Zero-Energy Buildings in Germany: Design, Model Calibration and Lessons Learned from a Case-Study in Berlin." *Energy and Buildings* 133:688–710.
- ASHRAE. 2013. "ANSI/ASHRAE Standard 169-2013 - Climatic Data for Building Design Standards." 98.
- Bhangar, S., N. A. Mullen, S. V. Hering, N. M. Kreisberg, and W. W. Nazaroff. 2011. "Ultrafine Particle Concentrations and Exposures in Seven Residences in Northern California." *Indoor Air* 21(2):132–44.
- Buonanno, G., L. Morawska, and L. Stabile. 2009. "Particle Emission Factors during Cooking Activities." *Atmospheric Environment* 43(20):3235–42.
- Candanedo, Luis M., Véronique Feldheim, and Dominique Deramaix. 2017. "Data Driven Prediction Models of Energy Use of Appliances in a Low-Energy House." *Energy and Buildings* 140:81–97.
- Caskey, Stephen L., Eric J. Bowler, and Eckhard A. Groll. 2016. "Analysis on a Net-Zero Energy Renovation of a 1920s Vintage Home." *Science and Technology for the Built Environment* 22(7):1060–73.
- Cetin, K. S., P. C. Tabares-Velasco, and A. Novoselac. 2014. "Appliance Daily Energy Use in New Residential Buildings: Use Profiles and Variation in Time-of-Use." *Energy and Buildings* 84:716–26.
- Derbez, Mickaël, Bruno Berthineau, Valérie Cochet, Céécile Pignon, Jacques Ribéron, Guillaume Wyart, Corinne Mandin, and Séverine Kirchner. 2014. "A 3-Year Follow-up of Indoor Air Quality and Comfort in Two Energy-Efficient Houses." *Building and Environment* 82:288–99.
- Diefenderfer, Philip, Peter Mark Jansson, and Edward R. Prescott. 2015. "Application of Power Sensors in the Control and Monitoring of a Residential Microgrid." *SAS 2015 - 2015 IEEE Sensors Applications Symposium, Proceedings*.

- De Hartog, J. J., G. Hoek, A. Peters, K. L. Timonen, A. Ibaldo-Mulli, B. Brunekreef, J. Heinrich, P. Tiittanen, J. H. Van Wijnen, W. Kreyling, M. Kulmala, and J. Pekkanen. 2003. "Effects of Fine and Ultrafine Particles on Cardiorespiratory Symptoms in Elderly Subjects with Coronary Heart Disease: The ULTRA Study." *American Journal of Epidemiology* 157(7):613–23.
- Hussein, Tareq, Thodoros Glytsos, Jakub Ondráček, Pavla Dohányosová, Vladimír Ždímal, Kaarle Hämeri, Mihalis Lazaridis, Jiří Smolík, and Markku Kulmala. 2006. "Particle Size Characterization and Emission Rates during Indoor Activities in a House." *Atmospheric Environment* 40(23):4285–4307.
- IEI. 2016. "Electric Company Smart Meter Deployments: Foundation for A Smart Grid." (December).
- Klepeis, Neil E., William C. Nelson, Wayne R. Ott, John P. Robinson, Andy M. Tsang, Paul Switzer, Joseph V. Behar, Stephen C. Hern, and William H. Engelmann. 2001. "The National Human Activity Pattern Survey (NHAPS): A Resource for Assessing Exposure to Environmental Pollutants." *Journal of Exposure Analysis and Environmental Epidemiology* 11(3):231–52.
- Newby, David E., Pier M. Mannucci, Grethe S. Tell, Andrea A. Baccarelli, Robert D. Brook, Ken Donaldson, Francesco Forastiere, Massimo Franchini, Oscar H. Franco, Ian Graham, Gerard Hoek, Barbara Hoffmann, Marc F. Hoylaerts, Nino Künzli, Nicholas Mills, Juha Pekkanen, Annette Peters, Massimo F. Piepoli, Sanjay Rajagopalan, and Robert F. Storey. 2015. "Expert Position Paper on Air Pollution and Cardiovascular Disease." *European Heart Journal* 36(2):83–93.
- Ng, Lisa, Dustin Poppendieck, W. Stuart Dols, and Steven J. Emmerich. 2018. "Evaluating Indoor Air Quality and Energy Impacts of Ventilation in a Net-Zero Energy House Using a Coupled Model." *Science and Technology for the Built Environment* 24(2):124–34.
- Oberdörster, G. 2001. "Pulmonary Effects of Inhaled Ultrafine Particles." *International Archives of Occupational and Environmental Health* 74(1):1–8.
- Oberdörster, Günter, Eva Oberdörster, and Jan Oberdörster. 2005. "Nanotoxicology: An Emerging Discipline Evolving from Studies of Ultrafine Particles." *Environmental Health Perspectives* 113(7):823–39.

- Panas, Alicja, Andreas Comouth, Harald Saathoff, Thomas Leisner, Marco Al-Rawi, Michael Simon, Gunnar Seemann, Olaf D??ssel, Sonja M??lhopt, Hanns Rudolf Paur, Susanne Fritsch-Decker, Carsten Weiss, and Silvia Diabat?? 2014. "HEI Perspectives 3: Understanding the Health Effects of Ambient Ultrafine Particles." *Beilstein Journal of Nanotechnology* 5(1):1590–1602.
- Peters, Annette, H. Erich Wichmann, Thomas Tuch, Joachim Heinrich, and Joachim Heyder. 1997. "Respiratory Effects Are Associated with the Number of Ultrafine Particles." *American Journal of Respiratory and Critical Care Medicine* 155(4):1376–83.
- Thomas, Walter D. and John J. Duffy. 2013. "Energy Performance of Net-Zero and near Net-Zero Energy Homes in New England." *Energy and Buildings* 67:551–58.
- Touchie, Marianne and Jeffrey Siegel. 2018. "Residential HVAC Runtime from Smart Thermostats: Characterization, Comparison, and Impacts." *Indoor Air* 0–2.
- US Department of Energy. 2011. "2011 Buildings Energy Databook." *Energy Efficiency & Renewable Energy Department* 286.
- US Department of Energy. 2015. *A Common Definition for Zero Energy Buildings*. edited by Intergovernmental Panel on Climate Change. Cambridge: Cambridge University Press.
- Voyvodic, James T. 2012. "Impact of Different Thermal Comfort Models on Zero Energy Residential Buildings in Hot Climate." *Journal of Magnetic Resonance Imaging: JMRI* 36(3):569–80.
- Wallace, Lance. 2006. "Indoor Sources of Ultrafine and Accumulation Mode Particles: Size Distributions, Size-Resolved Concentrations, and Source Strengths." *Aerosol Science and Technology* 40(5):348–60.
- Wallace, Lance A., Wayne R. Ott, Charles J. Weschler, and Alvin C. K. Lai. 2017. "Desorption of SVOCs from Heated Surfaces in the Form of Ultrafine Particles." *Environmental Science and Technology* 51(3):1140–46.
- Wallace, Lance, Fang Wang, Cynthia Howard-Reed, and Andrew Persily. 2008. "Contribution of Gas and Electric Stoves to Residential Ultrafine Particle Concentrations between 2 and 64 Nm: Size Distributions and Emission and Coagulation Rates." *Environmental Science and Technology* 42(23):8641–47.

- Yamada, Maromu, Mitsutoshi Takaya, and Isamu Ogura. 2015. "Performance Evaluation of Newly Developed Portable Aerosol Sizers Used for Nanomaterial Aerosol Measurements." *Industrial Health* 53(6):511–16.
- Zhang, Qunfang, Roja H. Gangupomu, David Ramirez, and Yifang Zhu. 2010. "Measurement of Ultrafine Particles and Other Air Pollutants Emitted by Cooking Activities." *International Journal of Environmental Research and Public Health* 7(4):1744–59.

VITA

Education

Master of Science in Civil Engineering at Purdue University, West Lafayette, Indiana, U.S., August 2017-present. Thesis: *Investigating How Energy Use Patterns Shape Indoor Nanoaerosol Dynamics in a Net-Zero Energy House*.

Bachelor of Science in Built Environment and Energy Engineering at Tongji University, Shanghai, China, September 2013-June 2017. Thesis: *Indoor Air Quality Investigation in 51 Residences in East and Central China and Ventilation Strategy Optimization*.

Publication

Yan Zhou, Hongwei Tan, Tingting Hu, **Jinglin Jiang**. Investigation and Analysis on the PM2.5 Concentration Distribution in a Campus in Shanghai. *Healthy Buildings 2017 Europe*, Lublin, Poland, July 2017.

Poster Presentation

Jinglin Jiang. Investigating How Energy Use Patterns Shape Indoor Nanoaerosol Dynamics in a Net-Zero Energy House. *2018 Herrick Industrial Advisory Committee (IAC) Meeting*, October 2018.

Awards & Honors

Learning Scholarship of Tongji University, Third Prize, 2015-2016.

Learning Scholarship of Tongji University, Second Prize, 2013-2014.